PHYSICAL REVIEW B **102**, 075308 (2020)

Finite-size effects in wave transmission through plasmonic crystals: A tale of two scales

Matthias Maier,[1,*] Mitchell Luskin,[2] and Dionisios Margetis[3]
[1]*Department of Mathematics, Texas A&M University, College Station, Texas 77843, USA*
[2]*School of Mathematics, University of Minnesota, Minneapolis, Minnesota 55455, USA*
[3]*Institute for Physical Science and Technology, and Department of Mathematics, and Center for Scientific Computation and Mathematical Modeling, University of Maryland, College Park, Maryland 20742, USA*

(Received 26 May 2020; revised 2 August 2020; accepted 5 August 2020; published 20 August 2020)

We study optical coefficients that characterize wave propagation through layered structures called plasmonic crystals. These consist of a *finite number* of stacked metallic sheets embedded in dielectric hosts with a *subwavelength spacing*. By adjustment of the frequency, spacing, number as well as geometry of the layers, these structures may exhibit appealing transmission properties in a range of frequencies from the terahertz to the mid-infrared regime. Our approach uses a blend of analytical and numerical methods for the distinct geometries with infinite, translation-invariant, flat sheets and nanoribbons. We describe the transmission of plane waves through a plasmonic crystal in comparison to an *effective dielectric slab* of equal total thickness that emerges from *homogenization*, in the limit of zero interlayer spacing. We demonstrate numerically that the replacement of the discrete plasmonic crystal by its homogenized counterpart can accurately capture a transmission coefficient akin to the extinction spectrum, even for a relatively small number of layers. We point out the role of a geometry-dependent *corrector field*, which expresses the effect of subwavelength surface plasmons. In particular, by use of the corrector we describe lateral resonances inherent to the nanoribbon geometry.

DOI: 10.1103/PhysRevB.102.075308

I. INTRODUCTION

In the past few years, the advent of two-dimensional (2D) materials with remarkable optoelectronic and thermal transport properties has revolutionized several aspects of nanophotonics [1–4]. In particular, doped monolayer graphene has an optical conductivity that allows this material to interact strongly with light in a wide range of frequencies, from the terahertz to the mid-infrared regime [5,6]. This feature has inspired novel designs of plasmonic devices and metamaterials with tunable optical properties [7–9].

Plasmonic crystals are a promising class of metamaterials. These structures consist of stacked metallic layers which are arranged parallel to each other with subwavelength spacing and are embedded in heterogeneous and anisotropic dielectric hosts. By the tuning of the frequency, electronic density, interlayer distance, or number of layers, plasmonic crystals may acquire unconventional optical properties [10–14]. To predict such properties, an approach is to model the crystal as an *effective continuous medium* [10,14,15]. This description may result from a *homogenization* procedure, in the asymptotic limit of vanishing interlayer spacing [16,17]. The validity and implications of this simplified description for plasmonic structures with a *finite, possibly small,* number of layers are the subjects of this paper. This focus distinguishes this work from the homogenization of periodic plasmonic structures of previous treatments [14,17].

In recent experiments, the transmission properties of stacks consisting of graphene sheets and insulators are measured or investigated at terahertz frequencies; see, e.g., [18–21]. A notable outcome is that an increase in the number of layers, say, from one to five, may cause a significant increase to the extinction spectrum of the structure [18]. For such a small number of layers, it is natural to wonder if the replacement of the inherently discrete, layered structure by a suitably determined continuous dielectric medium can allow for the accurate prediction of useful transmission properties. This issue lies at the heart of modeling photonic heterostructures and metamaterials of various geometries at the nanoscale [2,22–27].

In this paper, our goal is to address aspects of plasmonic metamaterials that may be intimately connected to experiments. We provide an answer to the following question of practical appeal: Can the homogenization procedure, which yields an effective continuous medium, provide accurate predictions for wave transmission through *layered* plasmonic structures with *prescribed* number of conducting sheets and geometries of physical and technological interest? Our approach is to apply homogenization theory in the (nonperiodic) setting of layered structures with *finite* thickness. This view enables us to study the effect of the number of layers, an experimentally controllable parameter, on optical properties of practical importance.

First, we consider the prototypical setting with translation-invariant, planar graphene sheets intercalated between isotropic and homogeneous dielectric hosts. For this configuration, we compute the Fresnel coefficients analytically in closed forms via the transfer-matrix approach for

---

[*] maier@math.tamu.edu; https://www.math.tamu.edu/~maier

transverse-magnetic (TM) polarization of the fields [28,29]. We also compare our findings to the respective homogenization results for structures of finite total thickness, adopting elements of a previous theory for periodic structures [14,30].

Second, we numerically examine the more realistic geometries with graphene nanoribbons embedded in dielectric hosts. This study is carried out by the following means: (i) the direct numerical computation of an appropriately defined transmission coefficient via the finite element method [31]; and (ii) the application of homogenization, which introduces the notion of the *corrector field* to the leading order in the interlayer spacing [17]. This field expresses the effect of the surface plasmon-polariton (SPP), a subwavelength mode that can be excited in 2D materials of suitably tuned conductivities. In this work, we combine the corrector field with the (finite) number of layers. This approach renders our treatment and results distinct from those in [17]. We show that the corrector field of the homogenized structure can keep track of microscale *lateral resonances* inherent to the actual geometry of a single nanoribbon. This surface wave interference effect is distinguished from *interlayer resonances*. The latter effect can also characterize the wave interaction between translation-invariant flat sheets at subwavelength spacing, when the corrector tends to vanish. Our numerics indicate possible discrepancies between predictions of the theory for the actual structure and the corresponding effective model.

Our approach is motivated by the need to develop physical insight as well as viable computational schemes for the design of complex nanophotonic devices. In particular, the homogenization theory captures signatures of microscale details in the form of weighted averages of material parameters such as the permittivity of the dielectric host and the surface conductivity of each sheet. In this framework, a structure that consists of a finite number of conducting sheets at adjustable spacing, and their dielectric hosts, is replaced by a suitably defined continuous medium (as the spacing tends to zero) with the same total thickness. Hence, the number of parameters and variables of the original problem is reduced in the effective model. However, the weight for the requisite averages is in principle provided by the corrector field which solves a boundary value problem in the appropriately defined "cell" or "representative volume element" [16,17]. This *cell problem* at the microscale is a key ingredient of periodic homogenization. Our goal here is to describe applications, advantages, as well as possible limitations of this simplified approach for the wave transmission through realistic plasmonic structures.

Surprisingly, we find that the leading-order, low-energy homogenization accurately captures the behavior of the relevant transmission coefficient as a function of frequency even for a small, less than 10, number of layers. In fact, the associated relative error can be negligible in situations of possibly practical interest, and decreases as inverse proportional to the number of layers (Secs. V and VI A). The analytical and numerical computation of discrete corrections to the homogenized result, due to the finite number of layers (or, finite interlayer spacing) in the structure, for two selected geometries and a wide range of frequencies is a highlight of our approach. These "finite-size" effects exemplify the pivotal role of the corrector field in the description of the effective dielectric medium if the sheets (i.e., nanoribbons in our study) are not translation invariant in 2D. This situation arises, for example, in the presence of edges or other defects on each sheet. In this setting, the cell problem is characterized by plasmonic lateral resonances, which we describe numerically. We reiterate that in the special case of translation-invariant layers, the corrector field vanishes identically. We compare our findings to previous theoretical models of similar flavor for plasmonic crystals (Sec. VI C).

Notably, our theoretical results for translation-invariant sheets here are found in qualitative agreement with past experiments using stacks with graphene sheets and insulators [18]. Furthermore, we point out that our predictions on microscale resonances in nanoribbon configurations can be experimentally testable (Sec. VI B). Bearing in mind possible practical considerations, we discuss the stability of our homogenization results under random perturbations of parameters (Sec. VI D).

Our work can be considered as an extension of previous studies that focused on the "epsilon-near-zero" (ENZ) condition in plasmonic heterostructures; see, e.g., [14,17,30,32–36]. One should recall that if the ENZ condition holds, it is theoretically possible for a wave to propagate along a specified direction of the crystal with almost no refraction at certain frequencies. In this paper, our results indicate that the ENZ condition is in principle immaterial in the assessment of the accuracy of the homogenized transmission coefficients. We note in passing that for a sufficiently large number of layers, which is not the main focus of this paper, the ENZ condition approximately characterizes the crossover between two distinct behaviors of the wave transmission versus frequency and number of layers (Sec. VI A). In seeking a connection of our computations to previous studies in plasmonic crystals [14,17,30,32–36], we analytically determine the behavior of the homogenized Fresnel coefficients for a plasmonic slab in the parameter regime where the ENZ condition is satisfied. In particular, we show how dissipation in the 2D material affects the homogenized result for wave transmission in this regime.

It is tempting to compare our transfer-matrix analysis for structures with translation-invariant sheets to the treatment of similar geometries for hyperbolic metamaterials in [10]; see also [37–40]. Here, we focus on the computation of Fresnel coefficients for wave transmission through layered structures. Hence, we do not address the dispersion relation of subwavelength ("high-k") surface modes that can be allowed by the layered structure [10]. In the Bloch wave theory, such modes manifest as singularities (poles) in the complex plane for the Fresnel coefficients as functions of the wave-vector component parallel to the sheets. The issue of how these singularities can be computed accurately in a homogenized model lies beyond our present scope. A related discussion, which touches upon plausible implications and extensions of our results, can be found in Sec. VI E.

We should alert the reader about other questions that are left open in our treatment. For example, we focus on the effects of TM-polarized fields, not addressing the case with transverse electric (TE) polarization. We do not study the effects that a nonlocal conductivity of the 2D material, say, like the one caused by viscous hydrodynamic electron flow [41], may have on the homogenization result. In our numerical computations, we adhere to the treatment of structures with *flat* conducting sheets; curved 2D materials would have to be the subject of a separate study. As we allude to above, our homogenization procedure is tailored to the treatment of relatively low wave numbers in the direction vertical to the sheets. The modification of this procedure to take into account interlayer wave phenomena at a length scale comparable to the subwavelength spacing is an interesting direction of research.

The remainder of the paper is organized as follows. In Sec. II, we apply the transfer-matrix approach to the computation of the Fresnel coefficients for a structure with a finite number of translation-invariant, flat metallic sheets. In particular, we derive the limit of these coefficients for small enough interlayer spacing. Section III focuses on the description of the Fresnel coefficients under the ENZ condition. In Sec. IV, we revisit the general homogenization framework for periodic layered structures, particularly the emergent corrector field, and then adopt the resulting effective permittivity for a plasmonic structure of finite thickness. Section V provides numerical results for plasmonic crystals in the distinct cases with translation-invariant sheets and nanoribbons in comparison to their homogenized counterparts. In Sec. VI, we discuss implications and extensions of our results. Section VII concludes the paper with a summary of the results. The Appendices provide technical yet nonessential derivations as well as a review of the general homogenization theory [17]. The time dependence is $e^{-i\omega t}$ throughout (ω is the angular frequency).

II. TRANSFER-MATRIX APPROACH: TRANSLATION-INVARIANT SHEETS

In this section, we apply the transfer-matrix formalism [28,29] to the calculation of the reflection and transmission coefficients for a plasmonic crystal with finite thickness under TM polarization of the electromagnetic field. The crystal consists of a finite number of infinitely extended sheets embedded in dielectric hosts, as shown in Fig. 1. The interlayer spacing of the structure is d, and the number of conducting sheets is $(N-1)$; thus, the total thickness is $H = Nd$. Each dielectric host and conducting sheet is translation invariant in y and z (but not in x). This geometry should be contrasted to the case with nanoribbons which is studied numerically in Sec. V (see also Sec. IV A for the respective Fresnel coefficients).

We assume that each sheet has the homogeneous and isotropic surface conductivity $\sigma(\omega)$. The dielectric host can be anisotropic with permittivity represented by the spatially constant matrix

$$\underline{\varepsilon}(\omega) = \mathrm{diag}(\varepsilon_x(\omega), \varepsilon_y(\omega), \varepsilon_z(\omega)),$$

where in general ε_ℓ are distinct ($\ell = x,\ y,\ z$). This anisotropic permittivity is necessary for the study at hand, particularly the computations of Sec. V. Our motivation for choosing this model for $\underline{\varepsilon}$ is twofold. First, anisotropic dielectric materials such as the hexagonal boron nitride (hBN) are of theoretical and experimental interest in plasmonics [8,9]. Second, the Fresnel coefficients derived in this section, in an anisotropic setting, are used in Sec. IV when the discrete system is replaced by an effective continuous medium (which is a single, macroscopically thick slab). In that case, the anisotropy in the effective description emerges from homogenization.

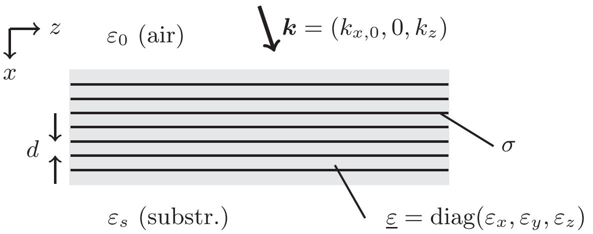

FIG. 1. Problem geometry. The layered structure has interlayer spacing d. The conducting sheets are isotropic with conductivity σ, and the dielectric host has tensor permittivity $\underline{\varepsilon} = \mathrm{diag}(\varepsilon_\perp, \varepsilon_{||}, \varepsilon_{||})$ in the indicated coordinate system. The structure lies between air (permittivity ε_0) and substrate (permittivity ε_s). All materials have uniform permeability μ. A plane wave (wave vector $\boldsymbol{k}$) is incident upon the structure from air.

The layered structure lies in the region with $0 < x < H$ between two unbounded, uniform dielectrics that have scalar permittivities ε_0 (for air) and ε_s (substrate). Thus, the free space and substrate occupy the regions with $x < 0$ and $x > H$, respectively. The magnetic permeability is equal to μ in all media.

A. Formulation

Assuming that the electromagnetic field $(\boldsymbol{E}, \boldsymbol{B})$ is TM polarized, we set $\boldsymbol{E} = (E_x, 0, E_z)$ and $\boldsymbol{B} = (0, B_y, 0)$ where all field components are y independent. Suppose that a plane wave is incident upon the layered structure from the air, for $x < 0$. This wave is partially reflected from and transmitted through the structure. In our configuration (Fig. 1), the z component k_z of the wave vector $\boldsymbol{k}$ of any associated plane wave is a prescribed invariant of the problem. In view of the fixed polarization, we can thus reduce the boundary value problem for Maxwell's equations for $(\boldsymbol{E}, \boldsymbol{B})$ to the transmission problem for a single field component, e.g., the z component E_z of $\boldsymbol{E}$ [14,31].

Hence, we aim to compute the related reflection and transmission coefficients by the following procedure. For every dielectric slab of the configuration, we write

$$E_z(x,z) = \mathcal{E}(x)\, e^{ik_z z}, \quad \mathcal{E}(x) = A\, e^{-ik_x x} + C\, e^{ik_x x},$$

where $\mathrm{Re}\, k_x > 0$ for definiteness. In the dielectric host, the wave number k_x is found to be

$$k_x = \sqrt{\frac{\varepsilon_{||}}{\varepsilon_\perp}\left(k_\perp^2 - k_z^2\right)} = \beta(k_z), \quad k_\perp^2 = \omega^2 \mu \varepsilon_\perp, \tag{1}$$

where $\varepsilon_\perp = \varepsilon_x$ and $\varepsilon_{=}\varepsilon_z$; see Appendix A for a derivation of dispersion relation (1) for k_x. For ease in notation, we henceforth denote the k_x in the host slab by β. Note that in the present case with TM polarization, the "lateral" matrix element ε_y of the diagonal $\underline{\varepsilon}$ becomes irrelevant; thus, we could have used the permittivity matrix $\underline{\varepsilon} = \mathrm{diag}(\varepsilon_\perp, \varepsilon_{,} \varepsilon_{)}$ without loss of generality.

The amplitudes A and C entering $\mathcal{E}(x)$ depend on the corresponding medium and layer, and can in principle be determined from the requisite transmission conditions, as outlined below. In particular, in air ($x < 0$) the field component E_z is expressed as

$$E_z^{\mathrm{air}} = \mathcal{E}^{\mathrm{air}}(x)\, e^{ik_z z}, \quad \mathcal{E}^{\mathrm{air}}(x) = e^{ik_{x,0} x} + R\, e^{-ik_{x,0} x},$$

where $k_{x,0} = \sqrt{k_0^2 - k_z^2}$ and $R(k_z)$ is the reflection coefficient with $k_0^2 = \omega^2\mu\varepsilon_0$. In the substrate ($x > H$), the solution for $E_z(x, z)$ becomes

$$E^{\rm sub} = \mathcal{E}^{\rm sub}(x)\, e^{ik_z z}, \quad \mathcal{E}^{\rm sub}(x) = T\, e^{ik_{x,\rm s} x},$$

where $T(k_z)$ is the transmission coefficient and $k_{x,\rm s} = \sqrt{k_{\rm s}^2 - k_z^2}$ with $k_{\rm s}^2 = \omega^2\mu\varepsilon_{\rm s}$.

The task at hand is to determine $R(k_z)$ and $T(k_z)$ explicitly. We thus apply the necessary boundary conditions through the dielectric interfaces and conducting sheets; see Appendix A for details. First, we impose continuity of $E_z(x, z)$ across each conducting sheet as well as across the interfaces of the dielectric host with air or substrate; thus, $\mathcal{E}(x)$ must be continuous at $x = nd$ for $n = 0, 1, \ldots, N$ [31]. Second, we require that the nonzero tangential (y) component of $\boldsymbol{B}$, which is proportional to $d\mathcal{E}/dx$, be continuous across the dielectric interfaces (at $x = 0, H$). In addition, this component must experience a *jump* equal to the surface current, σE_z, across each conducting sheet (at $x = nd$ for $n = 1, \ldots, N-1$) [31].

B. Formulas for Fresnel coefficients

Consider the layered structure of Fig. 1. We now address the full transmission problem by the transfer-matrix approach [28,29]. Here, we briefly outline the procedure, and state the main results for the Fresnel coefficients $R(k_z)$ and $T(k_z)$. Details of the derivation can be found in Appendix A.

The main idea is to view the whole transmission problem as a cascade of elementary propagation problems. We then connect the amplitudes of $E_z(x, z)$ for $x < 0$ and $x > H$ via the multiplication of the constituent transfer matrices. In this vein, we define the following matrices:

$$\mathcal{T}_{\rm I} = \begin{pmatrix} e^{-i\beta d} & 0 \\ 0 & e^{i\beta d} \end{pmatrix} = \mathcal{T}_{\rm I}(d),$$

$$\mathcal{T}_{\rm II} = \begin{pmatrix} 1 - \frac{id}{2\beta}[(\beta^{\rm eff})^2 - \beta^2] & -\frac{id}{2\beta}[(\beta^{\rm eff})^2 - \beta^2] \\ \frac{id}{2\beta}[(\beta^{\rm eff})^2 - \beta^2] & 1 + \frac{id}{2\beta}[(\beta^{\rm eff})^2 - \beta^2] \end{pmatrix},$$

where $\beta^{\rm eff}$ denotes the *effective* wave number

$$\beta^{\rm eff}(k_z) = \sqrt{\beta(k_z)^2 + i\,\frac{\omega\mu\sigma}{d}\,\frac{k_\perp^2 - k_z^2}{k_\perp^2}}. \tag{2}$$

In the above, $\mathcal{T}_{\rm I}$ characterizes the propagation of the z-directed electric field $\mathcal{E}(x)$ in the dielectric host by distance d. The matrix $\mathcal{T}_{\rm II}$ describes the transmission of $\mathcal{E}(x)$ through a sheet of surface conductivity σ that is immersed in the dielectric host at position $x = 0$ (see Appendix A). The effective wave number $\beta^{\rm eff}$ is introduced in hindsight, for later algebraic convenience: this definition serves our purpose of homogenizing the structure in the limit $\beta d \to 0$ by keeping certain nondimensional parameters fixed. The role of this $\beta^{\rm eff}$ becomes more clear in Sec. II C. In particular, we will require that $\beta^{\rm eff} H$ is independent of d as $\beta d \to 0$. This requirement is equivalent to the statement that σ scales linearly with d (or $\sigma/d \simeq$ const) if the other material parameters are considered as fixed [17]. The physical significance of this scaling of σ with d is discussed in Sec. II C.

By the transfer-matrix approach, the amplitude vector (A, C) for $\mathcal{E}(x)$ in the first slab with $0 < x < d$ is connected to the respective amplitudes in the last slab where $(N-1)d < x < H$. This is carried out by the successive application of $\mathcal{T}_{\rm I}(nd)$ and $\mathcal{T}_{\rm II}$ through the layered structure (for $n = 1, \ldots, N-1$). Subsequently, we have to relate the field amplitudes in the above extremal slabs to the pairs $(R, 1)$ and $(T, 0)$, in the air and substrate (see Fig. 1). To this end, we impose the continuity of E_z and B_y at $x = 0$ and H.

After some algebra, we arrive at the following closed-form expressions for the reflection and transmission coefficients R and T (see Appendix A):

$$\begin{cases} R = -\,\dfrac{\tilde{\varepsilon}_{\rm s+}\, t_{1-} - \tilde{\varepsilon}_{\rm s-}\, t_{2-}\, e^{i2\beta d}}{\tilde{\varepsilon}_{\rm s+}\, t_{1+} - \tilde{\varepsilon}_{\rm s-}\, t_{2+}\, e^{i2\beta d}}, \\ T = e^{-ik_{x,\rm s}H}\, e^{i\beta d}\, \dfrac{t_{1+}\, t_{2-} - t_{2+} t_{1-}}{\tilde{\varepsilon}_{\rm s+}\, t_{1+} - \tilde{\varepsilon}_{\rm s-}\, t_{2+}\, e^{i2\beta d}}. \end{cases} \tag{3}$$

Here, we define the matrix elements t_{ij} ($i,\ j = 1, 2$) by

$$\begin{pmatrix} t_{11} & t_{12} \\ t_{21} & t_{22} \end{pmatrix} = (\mathcal{T}_{\rm II}\mathcal{T}_{\rm I})^{N-1},$$

and also introduce the parameters

$$\tilde{\varepsilon}_{\ell\pm} = 1 \pm \frac{\varepsilon_\ell}{\varepsilon_\perp}\frac{k_\perp^2 - k_z^2}{\beta\, k_{x,\ell}} \quad \text{for } \ell = 0,\ \rm s,$$

$$t_{i\pm} = t_{i1}\, \tilde{\varepsilon}_{0\pm} + t_{i2}\, \tilde{\varepsilon}_{0\mp} \quad (i = 1,\ 2).$$

We note in passing that the analytical computation of the matrix elements t_{ij} can be carried out via the diagonalization of $\mathcal{T}_{\rm II}\mathcal{T}_{\rm I}$; see Appendices A and B. Specifically, by writing $\mathcal{T}_{\rm II}\mathcal{T}_{\rm I} = \mathcal{S}\,{\rm diag}(\lambda_+, \lambda_-)\mathcal{S}^{-1}$ where $\mathcal{S}$ is a nonsingular matrix and $\lambda_\pm$ are the eigenvalues of $\mathcal{T}_{\rm II}\mathcal{T}_{\rm I}$, we apply the identity

$$\begin{pmatrix} t_{11} & t_{12} \\ t_{21} & t_{22} \end{pmatrix} = \mathcal{S}\,{\rm diag}(\lambda_+^{N-1}, \lambda_-^{N-1})\,\mathcal{S}^{-1}.$$

Explicit formulas for $\mathcal{S}$ and $\lambda_\pm$ are given in Appendix B.

C. Limit of small interlayer spacing ($\beta d \to 0$)

Next, we illustrate the derivation of approximate formulas for the coefficients R and T in the limit as the number of layers N is sufficiently large ($N \gg 1$) and the interlayer spacing d is small enough. We discuss the underlying key assumptions in detail. In our limiting process the parameter $\beta H = N\beta d$ and the ratio σ/d are kept fixed (cf. [17]). The resulting limit formally expresses the homogenization of plasmonic crystals of finite thickness.

Specifically, a set of assumptions is described by [17]

$$|\beta d| \ll 1, \qquad \left|\frac{\omega\mu\sigma(\omega)}{\beta}\right| \ll 1,$$

with fixed βH. The first condition ($|\beta d| \ll 1$) means that d is small compared to the wavelength of propagation in the x direction inside the dielectric host. The second condition ($|\omega\mu\sigma/\beta| \ll 1$) implies the subwavelength character of the TM-polarized SPP associated with an *isolated* conducting sheet in the (unbounded) dielectric host. This condition expresses the separation of two distinct length scales: One scale is related to the wave number β describing the x-directed propagation in the dielectric slab, and another is related to the SPP wave number, which scales as $1/\sigma$ on the conducting sheet [14,17]. Note that TM-polarized SPPs cannot be excited on a single sheet by plane waves in the present geometry. Nonetheless, the above interpretation in terms of a scale separation helps us to point out the role of the spacing d, as we explain next.

In regard to the spacing d, we *additionally* assume that

$$\frac{\omega\mu\sigma(\omega)}{\beta^2 d} \simeq \text{const},$$

which means that the length $|\omega\mu\sigma(\omega)/\beta^2|$ scales linearly with d as $\beta d \to 0$. By Eq. (2), this assumption is compatible with $\beta^{\rm eff}H$ being kept fixed, independent of d. This choice of scaling for $\omega\mu\sigma(\omega)/\beta^2$ here implies that the wavelength of the TM-polarized SPP associated with the isolated sheet becomes comparable to the interlayer spacing. Hence, in the limit $\beta d \to 0$ the strength of the coupling of possible SPPs, or surface plasmonic modes, on neighboring sheets is nearly constant. The dimensionless parameter $\omega\mu\sigma/(\beta^2 d)$ expresses the strength of this coupling.

An alternative way to state the above scaling is to write

$$\sigma/d \simeq \text{const}$$

if the material parameters other than σ are considered as fixed, independent of d [17]. This choice of scaling σ linearly with d implies that the total surface current on the sheets remains *finite* in the limiting process ($\beta d \to 0$).

Without sacrificing the essential physics of the problem, for the sake of simplicity we set $\varepsilon_s = \varepsilon_0$. In other words, we assume that the whole layered structure is immersed in a homogeneous and isotropic medium (air). Consider normal incidence of the incoming plane wave, i.e., take $k_z = 0$.

Let us now turn our attention to the exact formulas of Eq. (3). By expanding the Fresnel coefficients in powers of βd, we obtain the following results to the leading order in βd (see Appendix B):

$$\begin{cases} R \simeq R^{\rm eff} = -\dfrac{\left[(\beta^{\rm eff})^2 - k_0^2\right]\tan(\beta^{\rm eff}H)}{\left[(\beta^{\rm eff})^2 + k_0^2\right]\tan(\beta^{\rm eff}H) + 2\,ik_0\beta^{\rm eff}}, \\[2ex] T \simeq T^{\rm eff} = \dfrac{e^{-ik_0H}\,2\,ik_0\beta^{\rm eff}\sec(\beta^{\rm eff}H)}{\left[(\beta^{\rm eff})^2 + k_0^2\right]\tan(\beta^{\rm eff}H) + 2\,ik_0\beta^{\rm eff}}. \end{cases} \tag{4}$$

These equations define the homogenized Fresnel coefficients for the layered medium of total thickness H. Equation (4) can be extended to the case with $k_z \neq 0$, i.e., oblique incidence of the plane wave from air. This extension in the effective Fresnel coefficients can be carried out by replacing k_0 by the wave number

$$\tilde{k}_0 \;=\; k_0\,\frac{k_0}{k_{x,0}}\,\frac{k_\perp^2 - k_z^2}{k_\perp^2}.$$

A few remarks on the above approximate formulas for R and T are in order. These coefficients suggest that the layered structure is effectively replaced by a continuous medium characterized by the wave number $\beta^{\rm eff}$ for propagation in the transverse (x) direction. By Eq. (2) with $k_z = 0$, we have

$$\beta^{\rm eff} = \beta^{\rm eff}(0) = \sqrt{k_\parallel^2 + i\,\frac{\omega\mu\sigma}{d}}; \quad k_\parallel = \omega\sqrt{\mu\varepsilon_\parallel}.$$

Accordingly, in this limit, the wave in the plasmonic structure encounters the effective dielectric permittivity $\underline{\varepsilon}^{\rm eff} = \mathrm{diag}(\varepsilon_\perp^{\rm eff}, \varepsilon_\parallel^{\rm eff}, \varepsilon_\parallel^{\rm eff})$, where $\varepsilon_\perp^{\rm eff} = \varepsilon_\perp$ and

$$\varepsilon_\parallel^{\rm eff} = \varepsilon_\parallel + i\,\frac{\sigma(\omega)}{\omega d}.$$

The emergent anisotropy of the effective dielectric permittivity $\underline{\varepsilon}^{\rm eff}$ is intrinsic to the structure geometry: As $\beta d \to 0$, the surface conductivities of individual sheets conspire to give rise to a bulk property (volume conductivity) that necessarily modifies only the *lateral* matrix elements of $\underline{\varepsilon}$ in the effective-medium description. More generally, geometric asymmetries between the transverse and lateral directions, relative to each layer, at the scale of the interlayer spacing d are expected to give rise to material anisotropy in the homogenization limit [16,17].

The results of this section are compatible with the dispersion relation derived via Bloch wave theory in [14,30] for a periodic array of conducting sheets. Recall that Eq. (3) is valid for infinite, translation-invariant layers. In this case, there are no (lateral) plasmonic resonances inherent to the geometry of the isolated 2D material. In contrast, each nanoribbon is characterized by resonances related to the strip width. These subtle effects of geometry are captured by the corrector field [17]. Regarding the general homogenization theory and the corrector field, the interested reader is referred to Sec. IV.

Numerical comparisons of a transmission property ("complementary transmission spectrum") related to the homogenized coefficients (4) to the exactly computed formula based on Eq. (3) indicate that the homogenization results are reasonably accurate. The accuracy persists even for a relatively small number N of layers. A quantitative study of this issue for the practically appealing cases [18] with $N = 4$, 8, and 16 is presented in Sec. V.

III. TRANSMISSION AT THE ENZ CONDITION

In this section, we describe the effect of a generalized ENZ condition on the homogenized coefficients of Eq. (4). In our setting (Fig. 1), the idea underlying this condition is suggested by the observation that a wave propagating in the effective medium of the plasmonic crystal in the (x) direction transverse to the layers can be suitably tuned to experience almost no phase delay [14,30].

This theoretical possibility is typically introduced for periodic plasmonic crystals without Ohmic losses (see, e.g, [30]). Our study here offers an extension of this concept to include finite-number-of-layers and dissipation effects. The possible role of the ENZ condition in the description of wave transmission through a plasmonic structure with a finite number of layers for a wide range of frequencies is discussed in Sec. VI A.

First, we review the concept of the ENZ condition in the absence of dissipation (for $\mathrm{Re}\,\sigma \simeq 0$). A means of arriving at the ENZ condition is to require that the effective wave number of Eq. (2) vanishes for any given k_z. Alternatively, at least one (real) eigenvalue of the effective permittivity tensor becomes zero [17]; here, this requirement yields $\varepsilon_\parallel^{\rm eff} = 0$. For periodic plasmonic crystals, this condition entails that a branch of the dispersion relation $k_x(k_z)$ for the layered structure approaches a Dirac cone near the center of the Brillouin zone [14,30].

More generally, if the dielectric media are lossless but each conducting sheet is *dissipative* ($\mathrm{Re}\,\sigma > 0$), we define the ENZ condition by

$$\mathrm{Re}\,\varepsilon_{\parallel}^{\mathrm{eff}} = 0 \;\Rightarrow\; \mathrm{Re}\left\{\varepsilon_{\parallel} + i\,\frac{\sigma(\omega)}{\omega d}\right\} = 0. \qquad (5)$$

This equation entails $d = (\mathrm{Im}\,\sigma)/(\omega\varepsilon_{\parallel})$. Assuming again normal incidence of the incoming plane wave, i. e., $k_z = 0$, as well as $\varepsilon_s = \varepsilon_0$, by Eqs. (2) and (5) we obtain

$$[\beta^{\mathrm{eff}}(0)]^2 = \frac{i\omega\mu(\mathrm{Re}\,\sigma)}{d} \;\Rightarrow\; \beta^{\mathrm{eff}} = \beta^{\mathrm{eff}}(0) = \gamma\, k_{\parallel},$$

where $k_{\parallel} = \omega\sqrt{\mu\varepsilon_{\parallel}} = \omega\sqrt{\mu\varepsilon}$ and

$$\gamma = e^{i\pi/4}\, k_{\parallel}^{-1}\sqrt{\frac{\omega\mu(\mathrm{Re}\,\sigma)}{d}} = (1+i)\sqrt{\frac{\mathrm{Re}\,\sigma}{2\,\mathrm{Im}\,\sigma}}.$$

In the above equation, we replaced d by $(\mathrm{Im}\,\sigma)/(\omega\varepsilon_{\parallel})$ according to the ENZ condition. The dimensionless complex parameter γ measures the effect of dissipation and indicates the deviation of condition (5) from its dissipation-free counterpart [14,30]. Typically, for a range of terahertz frequencies in doped monolayer graphene, we expect that $|\gamma| \ll 1$ [4]. Note that the symbol γ here should not be confused with the same symbol used typically to denote the (positive) damping figure of merit for SPPs [4]. Qualitatively, however, both quantities express the effect of dissipation; more precisely, $-i\gamma^2$ equals the standard SPP damping ratio [4].

We proceed to provide simplified formulas for R^{eff} and T^{eff} when condition (5) holds. Equation (4) yields

$$\begin{cases} R^{\mathrm{eff}} \to R_{\mathrm{ENZ}} = \dfrac{\left(k_0^2 - \gamma^2 k_{\parallel}^2\right)\tan(\gamma k_{\parallel} H)}{\left(k_0^2 + \gamma^2 k_{\parallel}^2\right)\tan(\gamma k_{\parallel} H) + 2i\gamma k_{\parallel} k_0}, \\[2ex] T^{\mathrm{eff}} \to T_{\mathrm{ENZ}} = \dfrac{e^{-ik_0 H}\, 2\, i\gamma k_0 k_{\parallel}\, \sec(\gamma k_{\parallel} H)}{\left(k_0^2 + \gamma^2 k_{\parallel}^2\right)\tan(\gamma k_{\parallel} H) + 2\, i\gamma k_0 k_{\parallel}}. \end{cases}$$

It is reasonable to assume that $k_{\parallel}H$ is fixed and not large (see Sec. II C). Thus, the smallness of $|\gamma|$ in *weakly dissipative* 2D materials should imply that $|\gamma k_{\parallel} H| \ll 1$. Accordingly, we can expand the coefficients R_{ENZ} and T_{ENZ} in powers of the parameter $\gamma k_{\parallel} H$. By expanding up to second order in this parameter, after some algebra we obtain

$$R_{\mathrm{ENZ}} \simeq \frac{k_0 H}{2\,i + k_0 H} + \frac{i\gamma^2}{(2\,i + k_0 H)^2}\left\{\frac{2}{3} - \frac{2 + 2i\,k_0 H}{(k_0 H)^2}\right\}(k_0 H)(k_{\parallel} H)^2$$

and

$$e^{ik_0 H}\, T_{\mathrm{ENZ}} \approx \frac{2\,i}{2\,i + k_0 H} - \frac{i\gamma^2}{(2\,i + k_0 H)^2}\left\{\frac{2}{3} - \frac{2i + k_0 H}{k_0 H}\right\}(k_0 H)(k_{\parallel} H)^2.$$

It is of interest to note that the above approximate relations entail

$$R_{\mathrm{ENZ}} + e^{ik_0 H} T_{\mathrm{ENZ}} \simeq 1 \quad \text{and} \quad |R_{\mathrm{ENZ}}|^2 + |T_{\mathrm{ENZ}}|^2 \simeq 1.$$

IV. HOMOGENIZATION THEORY, CORRECTOR FIELD, AND RESONANCES

In this section, we revisit the established general theory of homogenization for periodic layered plasmonic structures [14,17]. In this theory, the corrector field can encode subwavelength plasmonic resonances inherent to the geometry of the constituent 2D material. Although the general homogenization theory has already been derived in [17] for arbitrary geometries of 2D materials in periodic structures (Appendix C), it is now tailored to the computation of experimentally observable quantities for practically appealing configurations, e.g., layered structures with graphene nanoribbons.

We use a simplified set of material parameters for the dielectric host and conducting sheet. In Sec. IV A, we derive formulas for the homogenized Fresnel coefficients, by adopting ingredients of the general homogenization theory in the present case with structures of finite thickness. To avoid technical complications, we restrict our attention to models that yield a *diagonal effective* permittivity matrix under TM polarization (cf. Sec. II). The resulting formulas for the optical coefficients provide a nontrivial extension to their counterparts for infinite, translation-invariant sheets; cf. Eq. (4). The role of the corrector field is discussed in Sec. IV B.

More precisely, our procedure regarding the Fresnel coefficients consists of the following stages. First, we provide the effective permittivity tensor $\underline{\varepsilon}^{\mathrm{eff}}$ that results from the homogenization of a periodic array of conducting sheets with arbitrary geometry. For general configurations, this $\underline{\varepsilon}^{\mathrm{eff}}$ has been derived from a two-scale asymptotic expansion for the fields obeying Maxwell's equations in the limit $k_0 d \to 0$ [17]; alternatively, one may use the Bloch wave theory for simple enough geometries [14]. The methodology of asymptotic expansions has the advantage that it is not limited to plane-wave solutions. Second, we replace the layered plasmonic crystal (Fig. 1) by a single *homogenized* anisotropic dielectric slab that has the permittivity tensor $\underline{\varepsilon}^{\mathrm{eff}}$ and the same thickness as the layered structure. We then compute directly the corresponding, effective Fresnel coefficients R^{eff} and T^{eff} when $\underline{\varepsilon}^{\mathrm{eff}}$ is diagonal (Sec. IV A). The results of this computation are relevant to nanoribbons (Sec. V).

To simplify the exposition, we assume that $\varepsilon_0 = \varepsilon_s$. To avoid complications due to the microscale material parameters per se, we posit that the dielectric host has the (isotropic and homogeneous) permittivity $\underline{\varepsilon} = \mathrm{diag}(\varepsilon, \varepsilon, \varepsilon)$ and the conducting sheet has the scalar surface conductivity σ. The surface of the sheet is assumed to be smooth enough, having a uniquely defined normal vector at every point of its interior (away from the boundary). The sheet can have edges. We alert the reader that the generality of our homogenization result for $\underline{\varepsilon}^{\mathrm{eff}}$ mainly concerns the sheet geometry (see Appendix C). It can be shown that for a representative volume element of linear size equal to d in all directions (Fig. 2), the matrix elements of the effective permittivity $\underline{\varepsilon}^{\mathrm{eff}}$ take the form

$$\varepsilon_{ij}^{\mathrm{eff}} = \varepsilon\delta_{ij} - \frac{\sigma(\omega)}{i\omega d^3}\int_{\Sigma}[\boldsymbol{\tau}_j + \nabla_{\boldsymbol{\tau}}\chi_j(\boldsymbol{r})]\cdot \boldsymbol{e}_i\, d\boldsymbol{r}. \qquad (6)$$

Here, χ_i is the ith component of the corrector field $\boldsymbol{\chi}$ (further described below); Σ is the surface region of the conducting sheet inside the representative volume element; $\boldsymbol{r} = (x, y, z)$

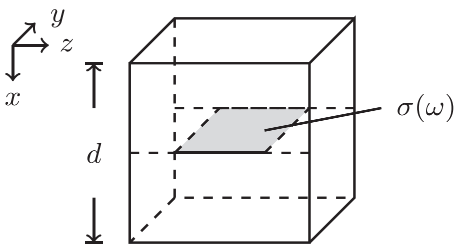

FIG. 2. Schematic of representative volume element (box) in nanoribbon configuration: the conducting strip lies in the yz plane, with each edge being parallel to the y axis. For the purpose of periodic homogenization, the representative volume element is repeated periodically with interlayer spacing equal to d (in the x direction).

and δ_{ij} is Kronecker's delta with $i,\ j = x,\ y,\ z$. To define the remaining quantities in Eq. (6), let $\boldsymbol{\nu}$ denote the (uniquely defined) unit vector normal to Σ. Accordingly, $\boldsymbol{\tau}_i(\boldsymbol{r})$ is the projection of the i-directed Cartesian vector $\boldsymbol{e}_i$ to the plane tangential to Σ at point $\boldsymbol{r}$, viz., $\boldsymbol{\tau}_i = \boldsymbol{e}_i - (\boldsymbol{e}_i \cdot \boldsymbol{\nu})\boldsymbol{\nu}$; and $\nabla_{\boldsymbol{\tau}}$ is the surface gradient on Σ, i.e., $\nabla_{\boldsymbol{\tau}} = \nabla - (\nabla \cdot \boldsymbol{\nu})\boldsymbol{\nu}$. Note that Σ is finite. In the special case where Σ is flat and lies on the yz plane, we have $\boldsymbol{\tau}_j \cdot \boldsymbol{e}_i = \delta_{ij}$ if $i,\ j = y, z$ and $\boldsymbol{\tau}_j \cdot \boldsymbol{e}_i = 0$ otherwise. Equation (6) describes a suitable weighted *average* over microscale (d-dependent) details. The weight is determined by the corrector field $\boldsymbol{\chi}$ which is determined by a Helmholtz-type boundary-value problem in the representative volume element (see Appendix C). This field captures fine-scale, low-order lateral plasmonic resonances that are possibly excited in the 2D material (see Sec. V C).

A. Homogenized Fresnel coefficients in TM polarization

Next, we use the general homogenization result (6) for $\underline{\varepsilon}^{\text{eff}}$ in order to compute the effective Fresnel coefficients of a layered plasmonic structure in the limit $k_0 d \to 0$ with finite total thickness (see Fig. 1). The incident plane wave is TM polarized. For the sake of simplicity, we focus on geometries for which the matrix $\underline{\varepsilon}^{\text{eff}}$ is diagonal, $\underline{\varepsilon}^{\text{eff}} = \text{diag}(\varepsilon_x^{\text{eff}}, \varepsilon_y^{\text{eff}}, \varepsilon_z^{\text{eff}})$, where possibly $\varepsilon_x^{\text{eff}} \neq \varepsilon_y^{\text{eff}} \neq \varepsilon_z^{\text{eff}} \neq \varepsilon_x^{\text{eff}}$. This case accounts for configurations with infinitely extended sheets, nanoribbons, and circular nanotubes [17]. Note that this type of anisotropic permittivity $\underline{\varepsilon}^{\text{eff}}$ may result even from the homogenization of isotropic dielectric hosts with conducting sheets. Numerical simulations based on our homogenization results for nanoribbons are presented in Sec. V.

The goal in this section is to replace the multilayer system of Fig. 1 by a single-layer, continuous medium with dielectric permittivity equal to $\underline{\varepsilon}^{\text{eff}}$. This medium is of course located between the air and dielectric substrate and has thickness equal to H. To calculate the coefficients R and T for TM polarization, we apply the transfer-matrix approach of Sec. II B with $N = 1$, $\varepsilon_\perp = \varepsilon_x^{\text{eff}}$, and $\varepsilon_\parallel = \varepsilon_z^{\text{eff}}$; thus, we replace d by H. Because of our assumption for a TM-polarized incident plane wave, the matrix element $\varepsilon_y^{\text{eff}}$ does not enter the calculation.

By inspection of the transfer-matrix procedure, we realize that we can invoke Eq. (3) with $t_{11} = t_{22} = 1$ and $t_{12} = t_{21} = 0$ (see Sec. II B). Consequently, we find

$$\begin{cases} R^{\text{eff}} \;=\; -\,\dfrac{\tilde{\varepsilon}_{\text{s}+}\,\tilde{\varepsilon}_{0-} - \tilde{\varepsilon}_{\text{s}-}\,\tilde{\varepsilon}_{0+}\,e^{i2\beta^{\text{eff}}H}}{\tilde{\varepsilon}_{\text{s}+}\,\tilde{\varepsilon}_{0+} - \tilde{\varepsilon}_{\text{s}-}\,\tilde{\varepsilon}_{0-}\,e^{i2\beta^{\text{eff}}H}}, \\[2ex] T^{\text{eff}} \;=\; e^{-ik_{x,\text{s}}H}\,\dfrac{\left(\tilde{\varepsilon}_{0+}^2 - \tilde{\varepsilon}_{0-}^2\right)e^{i\beta^{\text{eff}}H}}{\tilde{\varepsilon}_{\text{s},+}\,\tilde{\varepsilon}_{0+} - \tilde{\varepsilon}_{\text{s}-}\,\tilde{\varepsilon}_{0-}\,e^{i2\beta^{\text{eff}}H}}, \end{cases} \tag{7}$$

where $\tilde{\varepsilon}_{\ell\pm}$ ($\ell = 0,\ \text{s}$) are defined by

$$\tilde{\varepsilon}_{\ell\pm} \;=\; 1 \pm \frac{\varepsilon_\ell}{\varepsilon_\perp^{\text{eff}}}\,\frac{(k_\perp^{\text{eff}})^2 - k_z^2}{\beta^{\text{eff}}\,k_{x,\ell}}; \quad k_\perp^{\text{eff}} = \omega\sqrt{\mu\varepsilon_\perp^{\text{eff}}}$$

with $\varepsilon_\perp^{\text{eff}} = \varepsilon_x^{\text{eff}}$. We invoke the effective wave number

$$\beta^{\text{eff}} = \sqrt{\frac{\varepsilon_\parallel^{\text{eff}}}{\varepsilon_\perp^{\text{eff}}}\big[(k_\perp^{\text{eff}})^2 - k_z^2\big]}, \tag{8}$$

where $\varepsilon_\parallel^{\text{eff}} = \varepsilon_z^{\text{eff}}$.

We should point out that Eq. (7) is valid for a wide class of sheet geometries, subject to the diagonal character of $\underline{\varepsilon}^{\text{eff}}$, in contrast to Eq. (4). The main difference of the present model for $\underline{\varepsilon}^{\text{eff}}$ from its counterpart of the transfer-matrix approach (Sec. II) is the effect of the corrector field $\boldsymbol{\chi}$. The derivation of the effective Fresnel coefficients for a more general, homogeneous but nondiagonal $\underline{\varepsilon}^{\text{eff}}$ is tractable but nonessential for our scope.

It is worthwhile to check that the coefficients of Eq. (7) correctly reduce to the corresponding Fresnel coefficients for the fully translation-invariant sheets of Sec. II. In this case, the boundary value problem for $\boldsymbol{\chi}$ (Appendix C) yields $\boldsymbol{\chi} = 0$. By Eq. (6), we obtain $\varepsilon_x^{\text{eff}} = \varepsilon$ and $\varepsilon_z^{\text{eff}} = \varepsilon + i\sigma/(\omega d) = \varepsilon_y^{\text{eff}} = \varepsilon_\parallel^{\text{eff}}$. For normal incidence of the incoming plane wave ($k_z = 0$), we have

$$\beta^{\text{eff}} = \sqrt{\omega^2\mu\varepsilon_\parallel^{\text{eff}}} = \sqrt{\beta^2 + \frac{i\omega\mu\sigma}{d}},$$

where $\beta^2 = \omega^2\mu\varepsilon = k_\parallel^2$, by the notation of Eq. (1). The substitution of the above value for the effective wave number β^{eff} into Eq. (7) yields the homogenized Fresnel coefficients in agreement with Eq. (4) if $\varepsilon_0 = \varepsilon_{\text{s}}$.

B. Corrector field in nanoribbon geometry

We now illustrate the role of the corrector field $\boldsymbol{\chi}$ by choosing to focus on the nanoribbon configuration with an isotropic dielectric host (Fig. 2). In this geometry, as outlined in the context of the general homogenization theory (Appendix C), all components of $\boldsymbol{\chi}$ vanish identically except χ_z. Thus, by Eq. (6) the effective permittivity tensor is written as $\underline{\varepsilon}^{\text{eff}} = \text{diag}(\varepsilon_x^{\text{eff}}, \varepsilon_y^{\text{eff}}, \varepsilon_z^{\text{eff}})$ where

$$\varepsilon_x^{\text{eff}} = \varepsilon, \quad \varepsilon_y^{\text{eff}} = \varepsilon - \eta(\omega), \tag{9a}$$

$$\varepsilon_z^{\text{eff}} = \varepsilon - \eta(\omega)\,\frac{1}{d^2}\int_\Sigma [1 + \partial_z\chi_\parallel(\boldsymbol{r})]\,d\boldsymbol{r}. \tag{9b}$$

In the above, $\eta(\omega) = \frac{\sigma(\omega)}{i\omega d}$, which is further discussed in Sec. V, and the corrector $\chi_\parallel(\boldsymbol{r}) = \chi_z(\boldsymbol{r})$ solves the associated cell problem (Appendix C). More generally, if the dielectric host has permittivity tensor $\underline{\varepsilon} = \text{diag}(\varepsilon_\perp, \varepsilon_\parallel, \varepsilon_\parallel)$ with $\varepsilon_\perp \neq \varepsilon_\parallel$ then $\varepsilon \to \varepsilon_\perp$ in $\varepsilon_x^{\text{eff}}$ whereas $\varepsilon \to \varepsilon_\parallel$ in both $\varepsilon_y^{\text{eff}}$ and $\varepsilon_z^{\text{eff}}$. Let us recall that, for a TM-polarized incident plane wave, the

Fresnel coefficients $R^{\rm eff}$ and $T^{\rm eff}$ are only affected by the parameters $\varepsilon_x^{\rm eff}$ and $\varepsilon_z^{\rm eff}$. We should add the remark that Eqs. (9) are applicable to the configuration with infinite, translation-invariant sheets for $\chi_\parallel = 0$, if the media parameters are kept fixed.

The above corrector field $\chi_\parallel(\boldsymbol{r})$, in principle, encodes the response of the plasmonic microstructure to all possible surface excitations by local plane waves [17]. In particular, this response may include short-scale, subwavelength surface modes on the 2D material, which we interpret as *(lateral) SPP resonances* [42]. These modes are excited on the 2D material because of the ribbon edges, and its finite width, as the asymptotically "slow" macroscopic electromagnetic wave solution approaches a plane wave in the homogenization limit [17].

This interpretation is consistent with the following observation. In the special geometry with infinite, translation-invariant sheets (Sec. II), the conducting material does not admit such a surface excitation, and the corrector $\boldsymbol{\chi}(\boldsymbol{r})$ vanishes identically [17]. In principle, the absence of microscale surface excitations on the 2D material should be equivalent to a vanishing corrector for the cell problem; consequently, $\varepsilon_y^{\rm eff} = \varepsilon_z^{\rm eff} = \varepsilon_\parallel - \eta(\omega)\frac{1}{d^2}\int_\Sigma d\boldsymbol{r}$. In contrast, the configuration with nanoribbons shows a dominant influence of the corrector field $\chi_z(\boldsymbol{r})$ when the frequency ω is close to resonance frequencies; see Sec. V for numerical results.

V. COMPUTATIONAL RESULTS

In this section, we numerically compare a quantity, the complementary transmission spectrum (defined below), of a fully *layered* structure to the respective result of the homogenization procedure. Our goal is to quantitatively assess the accuracy of homogenized models for the computation of wave transmission through plasmonic crystals for frequencies and geometries of possible practical interest. Of particular significance in applications is the dependence of the optical coefficients on the number of layers [18], which we study in some detail below. We assume that the electromagnetic field has TM polarization.

We choose to focus on two geometries with conducting isotropic 2D materials. One configuration consists of infinite, mutually parallel sheets (Fig. 1) and another consists of nanoribbons (Fig. 2). The former setting serves as a "reference case" since it allows us to apply the exact results of the transfer-matrix approach from Sec. II. In this geometry, however, there are *no microscale lateral resonances*. In contrast, the nanoribbon configuration enables the appearance of such resonances; in the homogenization limit, these effects can be captured by the corrector field, as we show below. For the nanoribbon case, we solve the full Maxwell system for the electromagnetic field via the finite element method [31,42] and compare the result to the respective homogenization outcome through the numerical solution of the boundary-value problem for the corrector field (see Sec. IV). In both cases of layered configurations, we assume that the 2D material is doped monolayer graphene. The microstructure includes an isotropic dielectric host ($\varepsilon_\parallel = \varepsilon_\perp = \varepsilon$). The macroscopic structure of thickness H lies between vacuum and a dielectric substrate (with permittivity $\varepsilon_{\rm s} > \varepsilon_0$). All media are nonmagnetic ($\mu = \mu_0$ for definiteness).

A. Preliminaries

First, we outline the setup of our numerical computations. For the homogenized Fresnel coefficients, we make use of Eqs. (7), which in principle incorporate the effect of the vector valued corrector field $\boldsymbol{\chi}$, in conjunction with Eqs. (9). In the reference case (infinite planar sheets), the corrector field vanishes identically ($\boldsymbol{\chi} = 0$). Recall that ingredients of the homogenization theory for the nanoribbon geometry are spelled out in Sec. IV B.

We apply a nondimensionalization of the relevant equations. In particular, we use the following rescaling of key parameters:

$$\tilde{\omega} = \frac{\hbar\omega}{E_F}, \quad \tilde{k} = \frac{k}{k_0}, \quad \tilde{\sigma}(\tilde{\omega}) = \sqrt{\frac{\mu_0}{\varepsilon_0}}\,\sigma(\omega),$$

where $E_{\rm F}$ denotes the Fermi energy, k is any relevant wave number (e.g., $k_{\rm s}$, $k_\perp$, and $\beta^{\rm eff}$), $\hbar$ is the reduced Planck constant, and $\mu_0 = \mu$. We combine the above rescaling with the Drude model for the scalar surface conductivity of the (isotropic) 2D material [31]. Hence, we use the following dimensionless surface conductivity [31]:

$$\tilde{\sigma}_{\rm Drude}(\tilde{\omega}) = \frac{i\,\tilde{\omega}_{\rm p}}{\tilde{\omega} + i/\tilde{\tau}}, \quad \tilde{\omega}_{\rm p} = \frac{4\,e^2}{4\pi\varepsilon_0\hbar c_0} = 4\,\alpha.$$

Here, $\tilde{\tau} = (E_{\rm F}/\hbar)\tau$, τ is the (phenomenological) relaxation time of the Drude model, and α denotes the fine-structure constant; as usual, e stands for the elementary (electron) charge and c_0 is the speed of light in vacuum.

In our numerics, we choose to compute the quantity

$$\mathfrak{T}_{\rm c} = 1 - |T(\tilde{\omega})|^2, \tag{10}$$

which we refer to as the *the complementary transmission spectrum* for the layered plasmonic structure of interest. This $\mathfrak{T}_{\rm c}$ is akin (but not identical) to the extinction spectrum of layered structures, which is usually measured in experiments [18]. An advantage of using this $\mathfrak{T}_{\rm c}(\tilde{\omega})$ is that it satisfies the inequality $0 < \mathfrak{T}_{\rm c} < 1$. We compute $\mathfrak{T}_{\rm c}$ by (i) the transfer-matrix approach as well as the explicit homogenization formula for T (with zero corrector field) for the reference case (Sec. V B), and (ii) the numerical solution of the Maxwell system as well as the homogenization procedure with a corrector field for the nanoribbon configuration (Sec. V C).

We pay particular attention to the *deviation* of the homogenized version of $\mathfrak{T}_{\rm c}$ from the corresponding quantity for the original layered structure. We refer to this deviation as the *homogenization error*. Recall that, in the homogenized problem, the layered structure is replaced by a slab of equal total thickness with an effective continuous medium. We extend the definition of the homogenization error to the computation of resonance frequencies in the nanoribbon configuration (Sec. V C).

To illustrate the homogenization error computationally, we choose and fix the relevant material parameters as follows. The dielectric permittivity of the substrate is $\varepsilon_{\rm s} = 4.4\varepsilon_0$, while the medium above the layered structure is vacuum (with permittivity ε_0). The value for $\varepsilon_{\rm s}$ used here is typical for

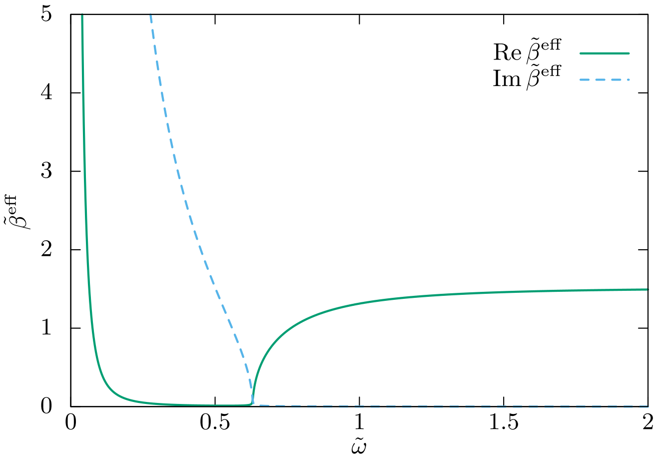

FIG. 3. Real and imaginary parts of rescaled, nondimensional effective wave number $\tilde{\beta}^{\rm eff}$ as a function of $\tilde{\omega}$ by Eq. (8), for the geometry with infinite planar sheets.

quartz [43]. We assume that the dielectric host is isotropic with $\varepsilon_\parallel = \varepsilon_\perp = 2.3\varepsilon_0$. This choice roughly corresponds to the permittivity values for polymer-based buffer materials in layered plasmonic structures, if one ignores the frequency dependence of the permittivity tensor $\underline{\varepsilon}$ [44].

By Eqs. (9) of the homogenization procedure, our parameter rescaling leads to the following weight for elements of the effective permittivity tensor [17]:

$$\tilde{\eta}(\tilde{\omega}) = \frac{\tilde{\omega}_p}{\tilde{\omega}^2(\tilde{\omega}+i/\tilde{\tau})\,\bar{d}},$$

where $\bar{d} = \tilde{d}/\tilde{\omega}$ and $\tilde{d} = k_0 d$; thus, $\bar{d}$ is frequency independent. In our numerical computations, we use the (dimensional) relaxation time $\tau = 0.4$ ps at the Fermi energy $E_{\rm F} = 0.4$ eV, which are typical for monolayer graphene. These choices imply the (nondimensional) parameter value $\tilde{\tau} = 243.2$. We also fix the interlayer spacing to $d = 25$ nm, which yields the parameter value $\bar{d} = 0.050\,68$. This choice of spacing is compatible with experiments on wave transmission through stacks consisting of graphene sheets and insulator slabs [18].

B. Infinite planar conducting sheets

Next, we carry out computations for the layered configuration of the reference case (Fig. 1). Our goal is to assess the accuracy of the homogenization results. In particular, we point out the negligible homogenization error even for small values of the number N of layers. We remind the reader that the (scaled) interlayer spacing $\bar{d}$ is kept fixed in our computations.

As a starting point, in Fig. 3 we show plots of the (N-independent) real and imaginary parts of the nondimensional effective wave number $\tilde{\beta}^{\rm eff} = \beta^{\rm eff}/k_0$ as a function of the rescaled frequency $\tilde{\omega}$. The parameter $\tilde{\beta}^{\rm eff}$ is computed by Eq. (8) with the appropriate, homogenized tensor permittivity.

In Fig. 4, we plot the complementary transmission spectrum $\mathfrak{T}_{\rm c}$ within the (exact) transfer-matrix approach as well as the (approximate) homogenization procedure. We consider $N = 4$, 8, and 16 layers. In these plots, the rescaled total thickness of the plasmonic structure is $\bar{H} = \bar{d}N = k_0 H$ where $H = Nd$ takes the values 100, 200, and 400 nm, respectively, as N varies. In Fig. 5, we show the relative homogenization error for the complementary transmission spectrum in a wide range of the (rescaled) frequency $\tilde{\omega}$.

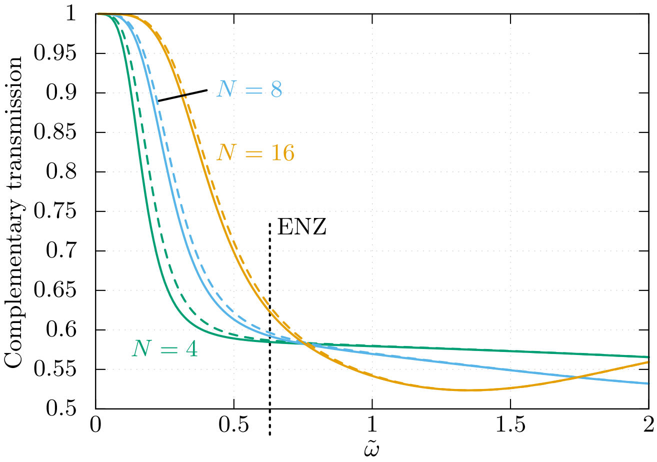

FIG. 4. Complementary transmission spectrum $\mathfrak{T}_{\rm c}$ for infinite planar sheets. The computations are carried out via transfer-matrix approach (solid line) and homogenization procedure (dashed line). We use $N = 4$, 8, 16 layers in each approach. The vertical dashed line indicates the ENZ condition.

A few remarks on the displayed numerical results are in order. Regarding Fig. 3, the ENZ condition is attained at the (N-independent) frequency $\tilde{\omega} \approx 0.63$. The computation of $T^{\rm eff}$ at the ENZ condition (Sec. III) gives a value for this coefficient in excellent agreement with the corresponding value shown in Fig. 4 (dashed curve). By inspection of Fig. 5, we see that the relative homogenization error remains well below 1% for a wide frequency range. A maximum relative error of about 10% occurs at $\tilde{\omega} \approx 0.2, 0.3, 0.46$ when $N = 4$, 8, 16, respectively. This error is seen to decrease almost inverse linearly with the number N of layers if N is sufficiently large. The local minimum in the complementary transmission spectrum for $N = 16$ (Fig. 4) can be attributed to an *interlayer resonance* (in the x direction), to be distinguished from the

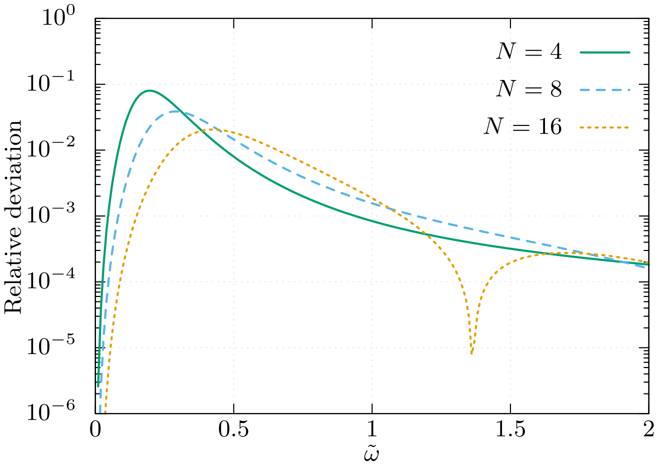

FIG. 5. Relative homogenization error for complementary transmission spectrum $\mathfrak{T}_{\rm c}$ for the geometry with infinite planar sheets. We use $N = 4$, 8, 16 layers.

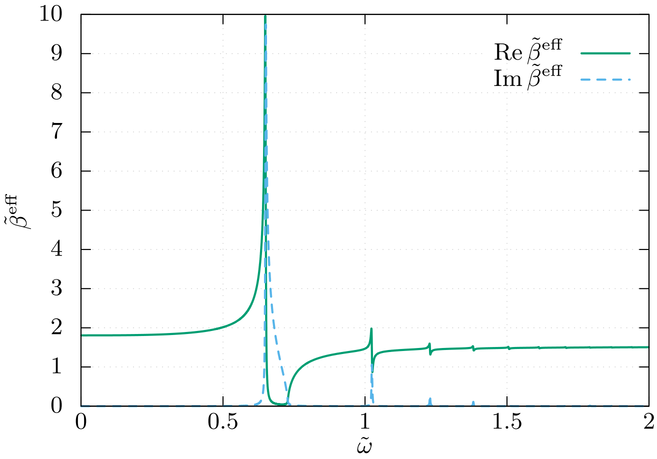

FIG. 6. Real and imaginary parts of rescaled, nondimensional effective wave number $\tilde\beta^{\rm eff}$ as a function of nondimensional frequency $\tilde\omega$ by Eq. (8), for the nanoribbon geometry.

lateral resonances of the nanoribbon geometry (Sec. V C). For increasing total thickness H, which scales linearly with N (for fixed spacing d), these resonances are shifted to lower frequencies. Indeed, by numerically computing $\mathfrak{T}_{\rm c}$ for the cases with $N = 32, 64, 128$, which are not displayed in the present plots, we observe roughly a doubling in the number of the above minima in the frequency range $0 \leqslant \tilde\omega \leqslant 2$ every time N is doubled. We expect this trend to persist for higher values of N.

C. Nanoribbon geometry

In this section, we study numerically the wave transmission through the layered structure that contains mutually parallel nanoribbons. In our numerical simulations, we set the width of each nanoribbon as well as the lateral spacing between nanoribbons in the yz plane equal to d. Hence, the representative volume element has a linear size equal to $2d$ in the z direction but the interlayer spacing is kept equal to d (cf. Fig. 2).

We compare outcomes of our numerics from two main approaches: One approach is the direct numerical solution of the full Maxwell system via the finite element method (for transmission through the layered configuration) [31], and another is the homogenization procedure (Sec. IV B). For the homogenized structure, the boundary-value problem for the corrector field $\boldsymbol{\chi}$ is solved numerically by the finite element method [17]. In this setting, we describe (lateral) SPP-related resonances inherent to each nanoribbon.

In Fig. 6, we plot the (N-independent) real and imaginary parts of the rescaled effective wave number $\tilde\beta^{\rm eff}$ as a function of the rescaled frequency $\tilde\omega$. The parameter $\tilde\beta^{\rm eff}$ is computed by Eq. (8) with the effective tensor permittivity of the nanoribbon geometry. In the present case, this computation involves a nontrivial corrector field.

The complementary transmission spectrum $\mathfrak{T}_{\rm c}$, computed by both the direct and homogenization approaches, is shown in Fig. 7. The numerical computations here are carried out for $N = 4$ and 8 layers. In Fig. 8, we display the relative homogenization error versus frequency $\tilde\omega$, in regard to the computation of $\mathfrak{T}_{\rm c}$ for each of the chosen values for N.

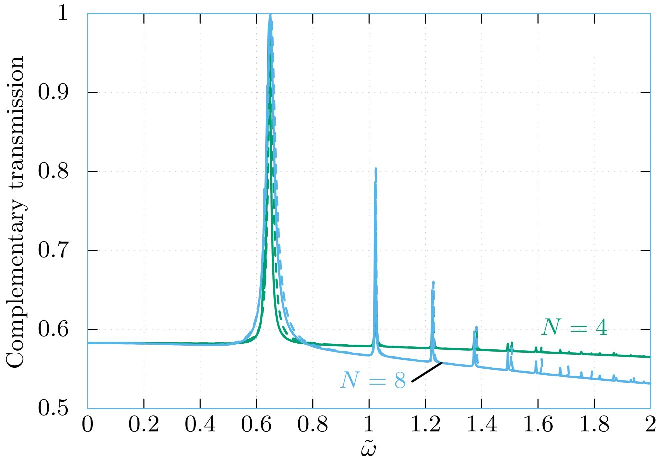

FIG. 7. Complementary transmission spectrum $\mathfrak{T}_{\rm c}$ for the nanoribbon geometry. The computations are carried out via numerical solution of transmission problem for fully layered structure (solid line) and homogenization procedure (dashed line). We use $N = 4,\ 8$ layers in each approach.

In our numerics, the lateral resonances manifest in the form of local peaks of the complementary transmission spectrum at certain frequencies, for fixed number N of layers; see Fig. 7. We reiterate that such resonances do *not* occur in the configuration with infinite conducting sheets (Sec. V B).

It is worthwhile to further quantify these lateral resonances. Let $\tilde\omega_n$ denote the relevant (nondimensional) resonance frequencies of the complementary transmission spectrum computed directly for the actual layered structure; n is a positive integer counting these frequencies in ascending order ($\tilde\omega_{n+1} > \tilde\omega_n$ with $n = 1,\ 2,\ \ldots$). Here, we set n equal to 1 for the lowest resonance frequency computed in our numerics. In Table I, we list the first eight ($n = 1,\ 2,\ \ldots,\ 8$) of these resonance frequencies, when the number of layers is $N = 4$ and 8.

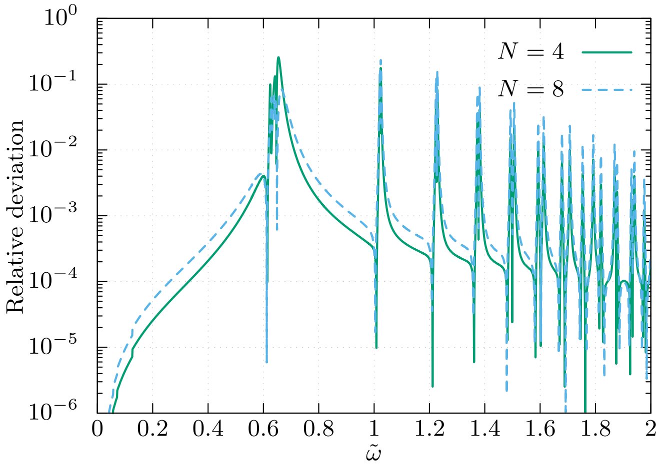

FIG. 8. Relative homogenization error for complementary transmission spectrum $\mathfrak{T}_{\rm c}$ for nanoribbon structure. We use $N = 4,\ 8$ layers.

TABLE I. First eight ($n = 1, 2, \ldots, 8$) resonance frequencies ($\tilde{\omega}_n$) for complementary extinction spectrum by distinct approaches and computations. Second column: frequencies $\tilde{\omega}_n^{\mathrm{eff}}$ of the homogenization approach. Third column: frequencies $\tilde{\omega}_n^{\mathrm{D}}$ of Dirichlet approximation for single nanoribbon. Last two columns: frequencies $\tilde{\omega}_n$ by direct numerical computation for layered structure with $N = 4$ and 8 layers. The percentages in parentheses of last three columns are the relative deviations of the computed frequencies from the respective homogenization results $\tilde{\omega}_n^{\mathrm{eff}}$.

n	$\tilde{\omega}_n^{\mathrm{eff}}$	$\tilde{\omega}_n^{\mathrm{D}}$	$\tilde{\omega}_n$ $(N = 4)$	$\tilde{\omega}_n$ $(N = 8)$
1	0.6501	0.7327 (13 %)	0.6446 (0.8%)	0.6484 (0.3%)
2	1.0237	1.0568 (3.2%)	1.0213 (0.2%)	1.0215 (0.2%)
3	1.2287	1.2530 (2.0%)	1.2241 (0.4%)	1.2242 (0.4%)
4	1.3814	1.4017 (1.5%)	1.3735 (0.6%)	1.3733 (0.6%)
5	1.5062	1.5242 (1.2%)	1.4928 (0.9%)	1.4928 (0.9%)
6	1.6130	1.6297 (1.0%)	1.5929 (1.2%)	1.5930 (1.2%)
7	1.7073	1.7230 (0.9%)	1.6788 (1.7%)	1.6789 (1.7%)
8	1.7920	1.8072 (0.8%)	1.7537 (2.1%)	1.7538 (2.1%)

We also compute the corresponding resonance frequencies $\tilde{\omega}^{\mathrm{eff}}$ from the homogenization approach. For this purpose, we locally fit a Lorentzian to the frequency response of the effective wave number $\tilde{\beta}^{\mathrm{eff}}(\tilde{\omega})$ near each resonance (see Fig. 6). We report the results in Table I.

We also provide the resonance frequencies $\tilde{\omega}_n^{\mathrm{D}}$ that come from the (N-independent) "Dirichlet approximation" pertaining to a single, *isolated* nanoribbon. This approximation is derived from the SPP excitation along a single conducting strip of finite width as follows (see Fig. 2): At the edges of the nanoribbon, impose homogeneous (zero) Dirichlet conditions to the generated unperturbed SPP, a suitable trigonometric function of z, for the z component of the electric field [42]. Accordingly, we find that the Dirichlet approximation $\tilde{\omega}_n^{\mathrm{D}}$ is obtained by the relation

$$\frac{\tilde{w}\big(\tilde{\omega}_n^{\mathrm{D}}\big)\,\tilde{k}_{\mathrm{spp}}\big(\tilde{\omega}_n^{\mathrm{D}}\big)}{2\pi} = \frac{2n-1}{2} \quad (n = 1, 2, \ldots), \tag{11}$$

where $\tilde{w}(\tilde{\omega}_n^{\mathrm{D}}) = \tilde{\omega}_n^{\mathrm{D}}\bar{d}$ is the width of an individual nanoribbon and

$$\tilde{k}_{\mathrm{SPP}}\big(\tilde{\omega}_n^{\mathrm{D}}\big) = \sqrt{\tilde{\varepsilon}_{\parallel} - \frac{4\,\tilde{\varepsilon}_{\parallel}^2}{\tilde{\sigma}\big(\tilde{\omega}_n^{\mathrm{D}}\big)^2}}$$

denotes the rescaled SPP wave number [42] at frequency $\tilde{\omega}_n^{\mathrm{D}}$. Here, $\tilde{\varepsilon}_{\parallel} = \varepsilon_{\parallel}/\varepsilon_0$ is the relative permittivity.

We close this section with a few more remarks on our numerics. An inspection of Fig. 8 indicates that the relative homogenization error (versus $\tilde{\omega}$) does not exceed about 1% for a wide frequency range. In fact, this deviation is exacerbated, with the relative error having local maxima in $\tilde{\omega}$ that may reach about 10%, near the resonance frequencies $\tilde{\omega}_n$. In regard to the calculation of the frequencies $\tilde{\omega}_n$, overall we observe a very good agreement between the directly computed values of these frequencies (for the actual layered structure) and their counterparts, $\tilde{\omega}_n^{\mathrm{eff}}$, for the homogenized problem. More precisely, the related deviation for $N = 8$ does not exceed 2.1% (see Table I). A close inspection of Fig. 7 reveals that the behavior of $\mathfrak{T}_{\mathrm{c}}$ near each resonance can be described (locally in $\tilde{\omega}$) by a Lorentzian, as expected [17]. The width of each Lorentzian depends on the dissipation, i.e., the real part of the surface conductivity $\sigma(\omega)$. According to the Drude model $\tilde{\sigma}_{\mathrm{Drude}}(\tilde{\omega})$ used here, this dissipation is controlled by the (rescaled) relaxation time $\tilde{\tau}$.

VI. DISCUSSION

In this section, we discuss implications of our study in the wave transmission through plasmonic structures. In particular, we point out the surprising accuracy of the homogenization approach in regard to the complementary transmission spectrum, and make an attempt to qualitatively compare our theoretical predictions to related experimental observations. Furthermore, we outline a possible extension of our study to the computation of waveguide modes in layered plasmonic structures with various sheet geometries.

A. Aspects of homogenized transmission

A central question motivating our computations is whether the homogenization of a layered plasmonic structure with finite thickness can yield sufficiently accurate results for the wave transmission. In the homogenization procedure, the error arises from the replacement of individual layers by a continuous medium through a delicate averaging process [cf. Eq. (6)]. The appropriate weight of the averaging in principle encodes microscale details (e.g., material edges). This weight is the corrector field.

We have assessed the accuracy of the homogenization results by numerically computing (i) the complementary transmission spectrum $\mathfrak{T}_{\mathrm{c}}$ as a function of frequency; and (ii) a few resonance frequencies $\tilde{\omega}_n$, that characterize the sheet geometry in the case with nanoribbons. We deem both $\mathfrak{T}_{\mathrm{c}}$ and $\tilde{\omega}_n$ as experimentally measurable.

In regard to $\mathfrak{T}_{\mathrm{c}}$, we observe that the relative homogenization error remains less than 1% for a wide range of frequencies, when the number N of layers is as small as 4. This error may reach a maximum of about 10% near frequencies that correspond to microscale resonances in the nanoribbon configuration. For fixed $\tilde{\omega}$, the error decreases almost inverse linearly with N.

The computed resonance frequencies $\tilde{\omega}_n$ ($n = 1, 2, \ldots, 8$) signify the influence on wave transmission of surface plasmons excited in the nanoribbon geometry. Notably, these frequencies are accurately captured within the homogenization approach via the numerical solution of the boundary-value problem for the corrector field. In general, the corresponding relative error ranges from 0.3% to 2.1% in our numerics. We notice that this error increases with the order n of the resonance. This behavior is a manifestation of an expected limitation of our homogenization approach: the averaging procedure underlying the homogenized formulas is valid to the leading order in the spacing $\bar{d}$, for slowly varying and low-energy incident plane waves. To achieve the same accuracy for high resonance frequencies ($n \gg 1$), one would need to properly modify the homogenization procedure. This task is left for future work (see also Sec. VI E).

It is worthwhile to comment on the role of the ENZ condition in the behavior of the complementary transmission spectrum $\mathfrak{T}_c$ for the structure with translation-invariant sheets (see Fig. 4). For fixed wave number k_z (tangential to each sheet), the frequency $\tilde{\omega}_{\text{ENZ}}$ coming from this condition tends to separate the frequency axis roughly into two regimes. For $\tilde{\omega} < \tilde{\omega}_{\text{ENZ}}$, the computed $\mathfrak{T}_c$ decreases with $\tilde{\omega}$ and can have appreciable values less than unity. In this range, if $\tilde{\omega}$ is kept fixed while N varies, $\mathfrak{T}_c$ is found to increase with N. On the other hand, for $\tilde{\omega} > \tilde{\omega}_{\text{ENZ}}$ (roughly), the computed $\mathfrak{T}_c$ may be nonmonotone and tends to become small; thus, wave transmission is enhanced. In this latter regime ($\tilde{\omega} > \tilde{\omega}_{\text{ENZ}}$), $\mathfrak{T}_c$ also loses its monotonicity with respect to N (for fixed $\tilde{\omega}$). These observations are consistent with the expected asymptotic behavior of $\mathfrak{T}_c$ for large enough values of N ($N > 100$), not used in our plots. More precisely, in this limit $\mathfrak{T}_c$ should approach a step function with values nearly equal to unity for $\tilde{\omega} < \tilde{\omega}_{\text{ENZ}}$ and close to zero otherwise. By this large-N picture, the character of the transmitted wave changes abruptly at the critical value $\tilde{\omega} = \tilde{\omega}_{\text{ENZ}}$: as $\tilde{\omega}$ decreases, the wave becomes evanescent below the "cutoff" frequency $\tilde{\omega}_{\text{ENZ}}$ because of the switch in the sign of the emerging effective permittivity.

Interestingly, we find hardly any connection of the ENZ condition to the extrema of the homogenization error for $\mathfrak{T}_c$, in the geometry with translation-invariant sheets (Figs. 3 and 5). Because of the absence of microscale (lateral) SPP-related resonances, this configuration is ideal for examining the frequency dependence of the homogenization error near the ENZ condition.

In the nanoribbon geometry, the behavior of the *macroscopic* quantity $\mathfrak{T}_c$ versus frequency is a direct consequence of the excitation of *fine-scale* SPPs on each sheet, because of the presence of material edges. These SPPs are encoded in the corrector field $\chi(\boldsymbol{r})$. Near each resonance frequency, $\chi(\boldsymbol{r})$ has a dominant contribution to the average of Eq. (6).

B. On the connection of theory to experiment

The setting of our study has been motivated by experiments of wave transmission through stacks with large, planar graphene sheets and insulator slabs [18]. Next, we briefly discuss how trends of our results can be directly connected to corresponding experimental observations.

First, the extinction spectrum measured in experiments is a decreasing function of frequency [see Figs. 2(a) and 2(b) in [18]]. This behavior is in agreement with the monotonicity of the computed $\mathfrak{T}_c$ for frequencies below ω_{ENZ} in the geometry with translation-invariant sheets; see our plots in Fig. 4.

Second, for fixed frequency the measured extinction spectrum increases with the number N of layers in the structure [Figs. 2(a) and 2(b) in [18]]. This monotonicity with N is also observed in our computations for $\mathfrak{T}_c$ when the sheets are translation invariant, provided the frequency range is such that $\omega < \omega_{\text{ENZ}}$ (Fig. 4).

Furthermore, we make predictions that can possibly be tested in future experiments with more complicated geometries. In particular, we mention our prediction of resonances in the wave transmission through the graphene nanoribbon configuration. An aspect of our computations that deserves attention for experimental designs is the possible tuning of the (lateral) SPP resonance through geometric or material parameters of the system. In this context, we highlight the role of the corrector field. Similar considerations should hold for other sheet geometries with edges and microscale defects.

C. Comparison to related homogenization results

The general homogenization result of [17], which provided the main ingredient of our present study, is primarily concerned with the derivation of an effective material property in the form of the permittivity tensor $\underline{\varepsilon}^{\text{eff}}$. This viewpoint is less concerned with establishing concrete dispersion relations for propagating modes. In the case with planar graphene sheets (Sec. II), the homogenization result is compatible with a dispersion relation derived via Bloch wave theory [14,30].

It is instructive to compare our effective permittivity tensor $\underline{\varepsilon}^{\text{eff}}$ to the corresponding effective permittivity that underlies the *Kronig-Penney model* for plasmonic crystals [45,46]. In these works, with reference to the coordinate system of Fig. 2, an arithmetic average is used to compute the matrix element $\varepsilon_z^{\text{eff}}$ while a harmonic mean is applied for $\varepsilon_x^{\text{eff}}$. This result holds true in the long-wavelength limit which is equivalent to our assumption that $\beta d \to 0$. The homogenization result is compatible with our Eq. (9) if the sheets are translation invariant. In this case, the harmonic and arithmetic means give the same result provided that the permittivity and conductivity are spatially constant. More generally, however, the main difference between the two results is that the role of the harmonic mean is replaced by a weighted arithmetic average governed by the corrector field $\chi_{\parallel}$ in our formalism. For example, the picture drastically changes from the situation of translation-invariant sheets when one introduces fine-scale lateral SPP resonances that do not vanish in the long-wavelength limit. This is the case for the nanoribbon configuration (Secs. IV and V): the resonances of Fig. 7 are solely caused by the corrector field and cannot be captured directly by a harmonic average.

D. Stability of the homogenization result under random perturbations

An important question concerns the stability of the homogenized Fresnel coefficients under some random variation of the problem parameters. A complete or rigorous answer to this question lies beyond our present scope. We are tempted, however, to present some brief heuristic arguments that address some notable cases. We mostly restrict our discussion to the stability of the entries of the effective permittivity tensor $\underline{\varepsilon}^{\text{eff}}$. The stability of related observable quantities such as the Fresnel coefficients can in principle be assessed from their respective formulas by applying the normal distribution for the error of $\underline{\varepsilon}^{\text{eff}}$. In this vein, we do not expect an error amplification [cf. Eqs. (7) and (8)]. We also do not address any homogenization errors beyond the finite-size effects that were already studied numerically in Sec. V.

Recall that the effective permittivity tensor $\underline{\varepsilon}^{\text{eff}}$ is given by Eq. (6). We heuristically distinguish two types of perturbations: (i) random variations that mainly influence the averaging procedure and change the corrector contribution negligibly; and (ii) random variations that change the corrector contribution appreciably. In the present setting of nanoscale resonators (conducting sheets intercalated in dielectrics), examples for type (i) include random variations of periodicity, alignment, and orientation that keep the shape and dimensions of the nanoscale resonator intact. In this case, we expect that the homogenization procedure is well controlled, and thus stable.

The situation is different for random variations of type (ii), which modify essential geometric features of the resonators. Examples for this type include random variations of the ribbon width, or the Drude weight of the surface conductivity. By revisiting the Dirichlet approximation (11) and Table I, we expect that the homogenization procedure remains stable as long as random variations for length scales under type (ii) are sufficiently smaller (in some sense) than the SPP wavelength: then, resonance frequencies will only shift slightly. Hence, it is reasonable to expect that random variations will only lead to slight broadening of the computed, unperturbed resonance behavior. (Regarding the complementary transmission spectrum, the unperturbed behavior is shown in Figs. 7 and 8).

E. Extension: Waveguide modes in plasmonic heterostructures

Our computational framework can be used to determine waveguide modes supported by plasmonic crystals of flat sheets at any given frequency ω. The objective is to obtain the wave number k_z as a function of ω (see Figs. 1 and 2). In principle, a multitude of such modes may exist for some fixed ω.

This problem is equivalent to searching for certain types of singularities (poles) in the Fresnel coefficients R and T as functions of the, in principle complex, variable k_z. A related question is how the resulting wave numbers k_z of the layered structure compare to their counterparts of the homogenized crystal. An appeal of our formalism is the incorporation of geometries other than translation-invariant sheets via the corrector field (cf. [10]).

To illustrate some of the technical aspects of determining $k_z(\omega)$, we turn our attention to Eqs. (3) and (7) which pertain to the Fresnel coefficients of the layered and homogenized structure, respectively. By setting equal to zero the denominator of Eq. (3), we obtain the dispersion relation

$$\tilde{\varepsilon}_{s+}\, t_{1+} - \tilde{\varepsilon}_{s-}\, t_{2+}\, e^{i2\beta d} = 0.$$

The admissible solutions $k_z^{\mathrm{lr}}(\omega)$ of this equation yield the lateral waveguide modes of the full layered structure. On the other hand, the homogenized dispersion relation is

$$\tilde{\varepsilon}_{s+}\, \tilde{\varepsilon}_{0+} - \tilde{\varepsilon}_{s-}\, \tilde{\varepsilon}_{0-}\, e^{i2\beta^{\mathrm{eff}}H} = 0,$$

with possible solutions $k_z^{\mathrm{hm}}(\omega)$. The question is how the values for $k_z^{\mathrm{lr}}(\omega)$ compare to those for $k_z^{\mathrm{hm}}(\omega)$. This question can be addressed numerically for distinct geometries. A detailed study lies beyond our present scope.

It turns out that the answer to the above question depends on the order of the mode, i.e., how high the value of $|k_z|$ needs to be for fixed ω. Because our homogenization procedure is valid for slowly varying and low-energy waves, it can provide reasonably accurate results for low values of $|k_z|$. In contrast, our homogenized results may become questionable for sufficiently large $|k_z|$. The situation regarding the homogenization error for k_z (for fixed ω) versus the mode number is analogous to that for $\tilde{\omega}_n$ versus n depicted in the last two columns of Table I.

These considerations point to the need for extending the homogenization procedure to high values of $|k_z|$. In the transfer-matrix approach, for translation-invariant sheets, we can seek this extension by relaxing the main assumptions of Sec. II C. More precisely, in the limit as $k_0 d \to 0$ we should assume that

$$|\beta d| \simeq \text{const}, \qquad \left|\frac{\omega\mu\sigma}{\beta}\right| \ll 1, \qquad \sigma/d \simeq \text{const}.$$

The first condition now replaces the previously applied statement $|\beta d| \ll 1$. The resulting expansions for R and T are deemed as manageable in this case.

For more general geometries, when the transfer-matrix approach is not directly applicable as above, the homogenization procedure needs a delicate modification to accommodate high values of $|k_z|$. In this case, microscale details of the conducting sheets are incorporated into the appropriate (nontrivial) corrector field. This problem is the subject of work in progress.

VII. CONCLUSION

In this paper, we studied analytically and numerically the wave transmission through plasmonic crystals for a wide range of frequencies. These structures consist of a *finite number* of mutually parallel conducting sheets intercalated between dielectric hosts, and are practically appealing. We computed the associated Fresnel coefficients by two alternate approaches. One method relies on direct computations for the full layered structure. Another approach makes use of homogenization, i.e., the replacement of the individual layers by an appropriately determined, in principle anisotropic, continuous medium in a slab of equal total thickness. We considered the two distinct geometries with infinite, translation-invariant sheets and nanoribbons.

Our results indicate the very good accuracy of the homogenized formula for the complementary transmission spectrum even for a relatively small number of layers. This result is a highlight of our analysis and numerics. In the case with nanoribbons, the maximum relative error occurs at SPP-related resonance frequencies. Notably, the first few (lowest) frequencies are captured accurately by the *corrector field* of the homogenization procedure which enters the effective permittivity tensor. This field incorporates effects from details of the microscale geometry, e.g., edges and defects. The use of the corrector in accurately identifying lateral resonances in layered plasmonic structures with finite total thickness is another noteworthy ingredient of our work.

A couple of open problems inspired by our work should be mentioned. It would be of interest to extend the computations to other configurations of possible experimental relevance such as those with flat microdisks or curved sheets. Another open task is that of a thorough stability analysis of the homogenization results under random variations of the problem parameters that would quantify the heuristic arguments of Sec. VI D. The homogenization procedure described here is applicable to low enough wave numbers. It must be properly modified to accurately capture effects of high wave numbers. This issue arises in the study of waveguide modes allowed to propagate through the plasmonic crystal. This problem deserves some attention.

ACKNOWLEDGMENTS

We wish to thank Prof. M. I. Weinstein, Prof. A. Alù, and Prof. P. Cazeaux for engaging discussions on homogenization and metamaterials. D.M. also thanks Prof. T. T. Wu for a discussion which motivated part of this work. The authors acknowledge partial support by the ARO MURI Award No. W911NF-14-1-0247. M.M. also acknowledges partial support by the NSF under Grant No. DMS-1912847. M.L. was also supported by the NSF under Grant No. DMS-1906129. The research of D.M. was also partially supported by a Research and Scholarship award by the Graduate School, University of Maryland. Part of this research was carried out when the authors were visiting the Institute for Pure and Applied Mathematics (IPAM), which is supported by NSF under Grant No. DMS-1440415.

APPENDIX A: DETAILS OF TRANSFER-MATRIX APPROACH

In this Appendix, we provide details for solving the full transmission problem of Sec. II via the transfer-matrix method. The incoming plane wave has TM polarization. First, we review the derivation of the dispersion relation $\beta(k_z)$ for the wave number in the x direction in the anisotropic medium of dielectric permittivity $\underline{\varepsilon}(\omega)$. Second, we sketch the steps for deriving explicit formulas for the Fresnel coefficients $R(k_z)$ and $T(k_z)$ that characterize the plane-wave propagation through the layered structure of Fig. 1. Our approach is based on applying a cascade of elementary transmission problems.

1. Derivation of dispersion relation $\beta(k_z)$

Let us first describe the dispersion of a TM-polarized plane wave propagating in a homogeneous anisotropic medium of permittivity $\underline{\varepsilon} = \mathrm{diag}\,(\varepsilon_x, \varepsilon_y, \varepsilon_z)$. Consider the following ansatz for the electric field:

$$\boldsymbol{E}(\boldsymbol{r}) = \boldsymbol{\mathcal{E}}\, e^{i\boldsymbol{k}\cdot\boldsymbol{r}},$$

where $\boldsymbol{k} = (k_x, k_y, k_z)$, $\boldsymbol{r} = (x, y, z)$, and $\boldsymbol{\mathcal{E}}$ is a constant vector. Maxwell's equations imply the statement

$$\boldsymbol{k} \times (\boldsymbol{k} \times \boldsymbol{\mathcal{E}}) + \omega^2 \mu \underline{\varepsilon}\, \boldsymbol{\mathcal{E}} \;=\; 0,$$

which must be solved for nonzero $\boldsymbol{\mathcal{E}}$.

For TM polarization, we write $\boldsymbol{\mathcal{E}} = (\mathcal{E}_x, 0, \mathcal{E}_z)$ and $\boldsymbol{k} = (\beta, 0, k_z)$. Hence, the above equation yields the system

$$\begin{pmatrix} \omega^2\mu\varepsilon_\perp - k_z^2 & \beta k_z \\ \beta k_z & \omega^2\mu\varepsilon_\parallel - \beta^2 \end{pmatrix} \begin{pmatrix} \mathcal{E}_x \\ \mathcal{E}_z \end{pmatrix} \;=\; 0,$$

where $\varepsilon_\perp = \varepsilon_x$ and $\varepsilon_\parallel = \varepsilon_z$. This linear system has a *nontrivial* solution $(\mathcal{E}_x, \mathcal{E}_z)$ if

$$(\omega^2\mu\varepsilon_\perp - k_z^2)(\omega^2\mu\varepsilon_\parallel - \beta^2) \;-\; \beta^2 k_z^2 \;=\; 0,$$

which yields Eq. (1) for $\beta(k_z)$ (see Sec. II).

2. Two elementary transmission problems

Next, we study two basic transmission problems in order to simplify the analysis for the full layered structure by the transfer-matrix approach. These problems are as follows: (i) propagation into an anisotropic dielectric of permittivity $\underline{\varepsilon}$ by a given distance; and (ii) transmission through a sheet of surface conductivity σ.

(i) Propagation in dielectric host by distance L. For algebraic convenience, we use the x-dependent part $\mathcal{E}(x)$ of the z component $E_z(x, z)$ of the electric field from Sec. II. At position $x = x_1$, this $\mathcal{E}(x)$ has the form

$$\mathcal{E}(x = x_1) = A^- e^{-i\beta x_1} + C^- e^{i\beta x_1}.$$

Hence, at position $x = x_2 = x_1 + L$ we have

$$\mathcal{E}(x = x_2) = A^+ e^{-i\beta x_1} + C^+ e^{i\beta x_1},$$

where

$$\begin{pmatrix} A^+ \\ C^+ \end{pmatrix} = \mathcal{T}_{\mathrm{I}}(L) \begin{pmatrix} A^- \\ C^- \end{pmatrix}, \quad \mathcal{T}_{\mathrm{I}}(L) \;=\; \begin{pmatrix} e^{-i\beta L} & 0 \\ 0 & e^{i\beta L} \end{pmatrix}. \tag{A1}$$

Recall that β is given by Eq. (1).

(ii) Transmission through conducting sheet. Suppose that a sheet with conductivity σ is situated at $x = 0$, between two dielectrics of permittivity $\underline{\varepsilon}$. Let us take

$$\mathcal{E}(x) = A^- e^{-i\beta x} + C^- e^{i\beta x}, \quad x < 0.$$

After transmission through the sheet, the related amplitudes change; thus, we have

$$\mathcal{E}(x) = A^+ c^{-i\beta x} + C^+ e^{i\beta x}, \quad x > 0.$$

We need to describe the matrix $\mathcal{T}_{\mathrm{II}}$ that connects (A^+, C^+) and (A^-, C^-).

For this purpose, let us consider the boundary conditions obeyed by the electromagnetic field across the sheet. First, $E_z(x, z)$ must be continuous at $x = 0$ [31]. Thus, we impose the condition

$$\mathcal{E}(0^+) - \mathcal{E}(0^-) = 0, \tag{A2}$$

where the statement $x = 0^+$ $(x = 0^-)$ means that x approaches 0 from above (below). In addition, the surface current density induced on the sheet causes a jump on the tangential component B_y of the magnetic field at $x = 0$. By use of Maxwell's equations we can express B_y in terms of E_z. Thus, we require that

$$\frac{i\omega\varepsilon_\perp}{k_\perp^2 - k_z^2} \left\{ \frac{d\mathcal{E}(0^+)}{dx} - \frac{d\mathcal{E}(0^-)}{dx} \right\} \;=\; \sigma\mathcal{E}(0), \tag{A3}$$

where $k_\perp^2 = \omega^2\mu\varepsilon_\perp$ (see Sec. II).

By replacing $\mathcal{E}(x)$ in Eqs. (A2) and (A3) by the formulas involving $A^\pm$ and $C^\pm$, we obtain the relation

$$\begin{pmatrix} A^+ \\ C^+ \end{pmatrix} = \mathcal{T}_{\mathrm{II}} \begin{pmatrix} A^- \\ C^- \end{pmatrix},$$

where

$$\mathcal{T}_{\mathrm{II}} \;=\; \begin{pmatrix} 1 + \frac{\omega\mu\sigma}{2\beta}\,\frac{k_\perp^2 - k_z^2}{k_\perp^2} & \frac{\omega\mu\sigma}{2\beta}\,\frac{k_\perp^2 - k_z^2}{k_\perp^2} \\ -\frac{\omega\mu\sigma}{2\beta}\,\frac{k_\perp^2 - k_z^2}{k_\perp^2} & 1 - \frac{\omega\mu\sigma}{2\beta}\,\frac{k_\perp^2 - k_z^2}{k_\perp^2} \end{pmatrix}. \tag{A4}$$

For later algebraic convenience, we choose to rewrite the above expression for transfer matrix $\mathcal{T}_{\mathrm{II}}$ in an alternate form by using the *effective* wave number

$$\beta^{\mathrm{eff}} = \beta\sqrt{1 + i\,\frac{\omega\mu\sigma}{\beta}\,\frac{1}{\beta d}\,\frac{k_\perp^2 - k_z^2}{k_\perp^2}}.$$

Recall that d denotes the interlayer spacing (see Fig. 1). The above definition of β^{eff} is motivated by the homogenization procedure of Sec. IV, where the ratio σ/d is treated as a (d-independent) constant if $|\beta d| \ll 1$ (see [14,17]). Accordingly, we obtain the expression

$$\mathcal{T}_{\mathrm{II}} = \begin{bmatrix} 1 - \frac{id}{2\beta}[(\beta^{\mathrm{eff}})^2 - \beta^2] & -\frac{id}{2\beta}[(\beta^{\mathrm{eff}})^2 - \beta^2] \\ \frac{id}{2\beta}[(\beta^{\mathrm{eff}})^2 - \beta^2] & 1 + \frac{id}{2\beta}[(\beta^{\mathrm{eff}})^2 - \beta^2] \end{bmatrix}.$$

3. Transmission through full multilayer system

Next, we sketch a derivation for the Fresnel coefficients $R(k_z)$ and $T(k_z)$ of the full layered structure (see Fig. 1). Our procedure relies on the successive application of results for the elementary problems (i) and (ii) stated above.

Let the field $\mathcal{E}(x)$ in a slab of the layered structure, for $(n-1)d < x < nd$, be described by

$$\mathcal{E}(x) = A^{(n)}\,e^{-ik_x x} + C^{(n)}\,e^{ik_x x},\ k_x = \beta;\ n = 1,\ \dots,\ N.$$

From Appendix A 2, the amplitudes $A^{(n)}$ and $C^{(n)}$ satisfy

$$\begin{pmatrix} A^{(n+1)} \\ C^{(n+1)} \end{pmatrix} = \{\mathcal{T}_{\mathrm{I}}(L)\}^{-1}\mathcal{T}_{\mathrm{II}}\mathcal{T}_{\mathrm{I}}(L)\begin{pmatrix} A^{(n)} \\ C^{(n)} \end{pmatrix}, \quad L = nd$$

if $n = 1,\ \dots,\ N-1$. Note the identity $\mathcal{T}_{\mathrm{I}}(md) = \{\mathcal{T}_{\mathrm{I}}(d)\}^m$ for any integer m. By successively applying the above recursive relation for $(A^{(n)}, C^{(n)})$, we obtain

$$\begin{pmatrix} A^{(N)} \\ C^{(N)} \end{pmatrix} = \mathcal{T}\begin{pmatrix} A^{(1)} \\ C^{(1)} \end{pmatrix},\ \mathcal{T} = \mathcal{T}_{\mathrm{I}}^{1-N}\,(\mathcal{T}_{\mathrm{II}}\mathcal{T}_{\mathrm{I}})^{N-1}, \tag{A5}$$

where the symbol $\mathcal{T}_{\mathrm{I}}$ stands for $\mathcal{T}_{\mathrm{I}}(d)$.

A remark on the analytical computation of the matrix $\mathcal{T}$ is in order. This calculation is carried out via the diagonalization of $\mathcal{T}_{\mathrm{II}}\mathcal{T}_{\mathrm{I}}$ (see also Appendix B). Accordingly, we explicitly determine the invertible matrix $\mathcal{S}$ such that $\mathcal{T}_{\mathrm{II}}\mathcal{T}_{\mathrm{I}} = \mathcal{S}\,\mathrm{diag}(\lambda_+, \lambda_-)\,\mathcal{S}^{-1}$ where $\lambda_\pm$ are the eigenvalues of $\mathcal{T}_{\mathrm{II}}\mathcal{T}_{\mathrm{I}}$. Clearly, this $\mathcal{S}$ is formed by eigenvectors of $\mathcal{T}_{\mathrm{II}}\mathcal{T}_{\mathrm{I}}$, which are calculable in closed form. Hence, we write

$$\mathcal{T} = \mathcal{T}_{\mathrm{I}}^{1-N}\mathcal{S}\,\mathrm{diag}(\lambda_+^{N-1}, \lambda_-^{N-1})\,\mathcal{S}^{-1},$$

where $\mathcal{T}_{\mathrm{I}}^{1-N} = \mathcal{T}_I((1-N)d)$. The formulas for $\mathcal{S}$ and $\lambda_\pm$ as well as an ensuing approximation for $\mathcal{T}$ if N is large and $\beta d \to 0$ are discussed in Appendix B.

The remaining task here is to relate the amplitudes $A^{(n)}$ and $C^{(n)}$ for $n = 1$ and N to coefficients R and T. Therefore, we need to apply the suitable transmission conditions at the corresponding interface between dielectric host and air or substrate, at $x = 0$ or $x = Nd = H$.

First, we consider the interface at $x = 0$. Recall that

$$\mathcal{E}(x) = \mathcal{E}^{\mathrm{air}}(x) = R\,e^{-ik_{x,0}\,x} + e^{ik_{x,0}\,x},\ x < 0$$

while $\mathcal{E}(x) = A^{(1)}e^{-i\beta x} + C^{(1)}e^{i\beta x}$ if $0 < x < d$. By requiring that the field components $E_z(x,z)$ and $B_y(x,z)$ be continuous at $x = 0$, we find that

$$\begin{cases} A^{(1)} + C^{(1)} = 1 + R, \\ \frac{i\omega\mu\varepsilon_\perp}{k_\perp^2 - k_z^2}(i\beta)(-A^{(1)} + C^{(1)}) = \frac{i\omega\mu\varepsilon_0}{k_{x,0}^2}(ik_{x,0})(-R+1). \end{cases}$$

This system yields

$$\begin{cases} A^{(1)} & = \frac{1}{2}\Big[1 + R - \frac{\varepsilon_0}{\varepsilon_\perp}\frac{k_\perp^2 - k_z^2}{k_{x,0}\beta}(1-R)\Big], \\ C^{(1)} & = \frac{1}{2}\Big[1 + R + \frac{\varepsilon_0}{\varepsilon_\perp}\frac{k_\perp^2 - k_z^2}{k_{x,0}\beta}(1-R)\Big]. \end{cases} \tag{A6}$$

Similarly, consider the interface at $x = H$. The transmitted wave is

$$\mathcal{E}(x) = \mathcal{E}^{\mathrm{sub}}(x) = T\,e^{ik_{x,\mathrm{s}}\,x},\ x > H = Nd$$

while $\mathcal{E}(x) = A^{(N)}e^{-i\beta x} + C^{(N)}e^{i\beta x}$ for $(N-1)d < x < H$. Accordingly, we obtain the system

$$\begin{cases} A^{(N)}\,e^{-i\beta Nd} + C^{(N)}\,e^{i\beta ND} \ = \ T\,e^{ik_{x,\mathrm{s}}Nd}, \\ \frac{i\omega\mu\varepsilon_\perp}{k_\perp^2 - k_z^2}(i\beta)(-A^{(N)}\,e^{-i\beta Nd} + C^{(N)}\,e^{i\beta ND}) \\ = \frac{i\omega\mu\varepsilon_{\mathrm{s}}}{k_{x,\mathrm{s}}^2}(ik_{x,\mathrm{s}})T\,e^{ik_{x,\mathrm{s}}Nd} \end{cases}$$

which entails

$$\begin{cases} A^{(N)} & = \frac{T}{2}e^{i(\beta + k_{x,\mathrm{s}})H}\Big(1 - \frac{\varepsilon_{\mathrm{s}}}{\varepsilon_\perp}\frac{k_\perp^2 - k_z^2}{\beta k_{x,\mathrm{s}}}\Big), \\ C^{(N)} & = \frac{T}{2}e^{i(-\beta + k_{x,\mathrm{s}})H}\Big(1 + \frac{\varepsilon_{\mathrm{s}}}{\varepsilon_\perp}\frac{k_\perp^2 - k_z^2}{\beta k_{x,\mathrm{s}}}\Big). \end{cases} \tag{A7}$$

After some algebra, Eqs. (A5)–(A7) yield the Fresnel coefficients $R(k_z)$ and $T(k_z)$. The resulting formulas are displayed compactly in Eq. (3) (Sec. II).

APPENDIX B: DERIVATION OF HOMOGENIZED SYSTEM VIA TRANSFER-MATRIX APPROACH

In this Appendix, we outline the derivation of the homogenized Fresnel coefficients R^{eff} and T^{eff} in the limit of small interlayer spacing d, as $\beta d \to 0$. To this end, we use the framework of Appendix A.

Accordingly, we can write

$$\mathcal{T}_{\mathrm{II}}\mathcal{T}_{\mathrm{I}} \ = \ \mathcal{S}\begin{pmatrix} \lambda_+ & 0 \\ 0 & \lambda_- \end{pmatrix}\mathcal{S}^{-1},$$

where $\mathcal{S}$ is a suitable nonsingular matrix and $\lambda_\pm$ are the two eigenvalues of $\mathcal{T}_{\mathrm{II}}\mathcal{T}_{\mathrm{I}}$. A direct computation for $\lambda_\pm$ under the conditions

$$|\beta d| \ll 1, \quad \left|\frac{\omega\mu\sigma}{\beta}\right| \ll 1, \quad \sigma/d \simeq \mathrm{const}$$

yields the formula

$$\lambda_\pm \ \simeq \ e^{\pm i\beta^{\mathrm{eff}}d}; \quad \beta^{\mathrm{eff}} = \sqrt{\beta^2 + \frac{i\omega\mu\sigma}{d}\,\frac{k_\perp^2 - k_z^2}{k_\perp^2}}.$$

Recall that the effective wave number β^{eff} was introduced in Eq. (2) in an *ad hoc* fashion. After some algebra, the transformation matrix $\mathcal{S}$ can be written as

$$\mathcal{S} = \begin{pmatrix} \check{\beta}\,e^{i\beta d} & \check{\beta}\,e^{i\beta d} \\ \lambda_+ - (1 + \check{\beta})e^{i\beta d} & \lambda_- - (1 + \check{\beta})e^{i\beta d} \end{pmatrix},$$

where $\check{\beta} = \frac{id}{2\beta}\{\beta^2 - (\beta^{\mathrm{eff}})^2\}$. A small-$d$ expansion for

$$\begin{bmatrix} t_{11} & t_{12} \\ t_{21} & t_{22} \end{bmatrix} = [\mathcal{T}_{\mathrm{II}}\mathcal{T}_{\mathrm{I}}]^{N-1} = \mathcal{S}\begin{pmatrix} \lambda_+^{N-1} & 0 \\ 0 & \lambda_-^{N-1} \end{pmatrix}\mathcal{S}^{-1}$$

furnishes the formulas

$$t_{11} \simeq \cos(\beta^{\mathrm{eff}}H) - i\,\frac{\beta^2 + (\beta^{\mathrm{eff}})^2}{2\beta\beta^{\mathrm{eff}}}\,\sin(\beta^{\mathrm{eff}}H),$$

$$t_{12} = -t_{21} \simeq -i\,\frac{(\beta^{\mathrm{eff}})^2 - \beta^2}{2\beta\beta^{\mathrm{eff}}}\,\sin(\beta^{\mathrm{eff}}H),$$

$$t_{22} \approx \cos(\beta^{\mathrm{eff}}H) + i\,\frac{\beta^2 + (\beta^{\mathrm{eff}})^2}{2\beta\beta^{\mathrm{eff}}}\,\sin(\beta^{\mathrm{eff}}H).$$

The homogenized coefficients of Eq. (4) are obtained by substitution of the above approximations for t_{ij} into Eq. (3), and the simplifications $k_z = 0$ and $\varepsilon_{\mathrm{s}} = \varepsilon_0$.

APPENDIX C: GENERAL PERIODIC HOMOGENIZATION

In this Appendix, we review the general homogenization result for periodic plasmonic crystals [17]. The underlying methodology relies on two-scale asymptotic expansions for solutions of the time-harmonic Maxwell equations. The main assumptions can be stated as follows. First, the material has a suitable periodic microstructure. This means that material parameters such as the permittivity of the dielectric host and the surface conductivity of the sheets have a well-defined microscopic periodicity which can be expressed via a representative volume element (cell) (see Fig. 2). This element is repeated periodically in all spatial directions; in particular, in the x direction its length is d which signifies the microscale size.

Second, a *separation of length scales* has to occur. In this regard, recall the hypotheses of Sec. II C. The main assumption of scale separation is that the wavelength of plane-wave propagation in air (with wave number k_0) is much larger than the length scale of the TM-polarized SPP on the single sheet. The latter length scales linearly with σ [4,31] and should be of the order of d here. Hence, we apply the familiar conditions (see Sec. II C)

$$|\beta d| \ll 1, \quad \left|\frac{\omega\mu\sigma}{\beta}\right| \ll 1, \quad \sigma/d \simeq \text{const}.$$

Consequently, the layered plasmonic crystal can be replaced by an appropriate continuous anisotropic medium which has an effective permittivity tensor $\underline{\varepsilon}^{\mathrm{eff}}$ [17]. The formula for this $\underline{\varepsilon}^{\mathrm{eff}}$ in principle contains (i) a weighted bulk average of the permittivity $\underline{\varepsilon}$ of the dielectric host, and (ii) a similarly weighted surface average of the conductivity σ of the 2D material. The weights for these averages depend on a (local) fine-scale, vector-valued corrector field $\boldsymbol{\chi}$, defined in the representative volume element (Fig. 2) [17]. This $\boldsymbol{\chi}$ satisfies a boundary-value problem in the representative volume element; the boundary conditions account for wave transmission through the arbitrarily shaped conducting sheet. In the present case, where $\underline{\varepsilon} = \mathrm{diag}(\varepsilon, \varepsilon, \varepsilon)$ describes the permittivity microstructure, the bulk average contribution trivially reduces to $\underline{\varepsilon}$ [17]. In contrast, the surface average can be complicated for arbitrary sheet geometry. More precisely, we obtain the following formula for the effective-permittivity matrix elements [17]:

$$\varepsilon_{ij}^{\mathrm{eff}} = \varepsilon\delta_{ij} - \frac{\sigma(\omega)}{i\omega d^3}\int_{\Sigma}[\boldsymbol{\tau}_j + \nabla_{\boldsymbol{\tau}}\chi_j(\boldsymbol{r})]\cdot\boldsymbol{e}_i\,d\boldsymbol{r}, \tag{C1}$$

where $i,\ j = x,\ y,\ z$; cf. Eq. (6). Each scalar field $\chi_i(\boldsymbol{r})$ is a potential-type function that is periodic in the representative volume element and encodes features (e.g., edges) of the sheet geometry. Therefore, χ_i captures fine-scale lateral plasmonic resonances that are possibly excited in the 2D material. By asymptotics, we have obtained the governing differential equation and associated boundary conditions for $\chi_i(\boldsymbol{r})$ [17]. In particular, in the interior of the representative volume element but outside the sheet Σ, the field $\chi_i(\boldsymbol{r})$ solves the Laplace equation, viz.,

$$\Delta\chi_i(\boldsymbol{r}) = 0; \tag{C2}$$

$\Delta = \partial^2/\partial x^2 + \partial^2/\partial y^2 + \partial^2/\partial z^2$ denotes the Laplacian.

In addition, χ_i obeys two transmission conditions across Σ. First, the field $\chi_i(\boldsymbol{r})$ must be continuous across Σ; thus, its tangential derivatives also are. This continuity condition ensures that the tangential electric field is continuous on Σ. Second, the normal derivative of χ_i has a jump discontinuity proportional to σ across Σ, viz.,

$$\boldsymbol{\nu}\cdot[(\nabla\chi_i)^+ - (\nabla\chi_i)^-] = \frac{\sigma(\omega)}{i\omega\varepsilon}\nabla_{\boldsymbol{\tau}}\cdot(\boldsymbol{\tau}_i + \nabla_{\boldsymbol{\tau}}\chi_i) \tag{C3}$$

on Σ. In the above, $\boldsymbol{Q}^{\pm}$ denotes the value of the vector $\boldsymbol{Q}$ on a prescribed side ($\pm$) of the *oriented* surface Σ, where by convention the vector $\boldsymbol{\nu}$ points outward the "+" side. Eq.s (C3) entails that the electric field normal to the conducting sheet experiences a jump proportional to the surface charge density on Σ. This condition also accounts for the jump of the tangential magnetic field due to the surface current density on Σ. Note that the term containing $\nabla_{\boldsymbol{\tau}}\cdot\boldsymbol{\tau}_i$ in Eq. (C3) can play the role of a forcing for the Laplace Eq. (C2). This term can be nonzero on a nonplanar surface Σ (e.g., a circular nanotube).

Another boundary condition for χ_i arises from the requirement that the electric field normal to possible edges of the conducting sheet must vanish [42]. This condition can be written as

$$\boldsymbol{n}\cdot(\boldsymbol{\tau}_i + \nabla_{\boldsymbol{\tau}}\chi_i) = 0 \quad \text{along edge}, \tag{C4}$$

where $\boldsymbol{n}$ is the outward-pointing unit vector normal to the edge and tangential to the surface Σ. By this condition, the term proportional to $\boldsymbol{n}\cdot\boldsymbol{\tau}_i$ can play the role of a forcing for the Laplace equation obeyed by χ_i, if the edge is present and $\boldsymbol{n}\cdot\boldsymbol{\tau}_i \neq 0$ (e.g., for a nanoribbon). Equation (C4) holds in the absence of a line charge density along the edge; see the discussion and extension in [17].

We can provide a plausibility argument for the microscale character of $\chi_i(\boldsymbol{r})$ by recalling our scaling hypothesis $\sigma/d \simeq$ const. By assuming that $\chi_i(\boldsymbol{r})$ depends on $\boldsymbol{r}/d$ and nondimensionalizing spatial coordinates, we realize that σ/d appears on the right-hand side of Eq. (C3). Thus, this condition is independent of d (as $k_0 d \to 0$).

A few remarks on the geometry with nanoribbons are in order (see Fig. 2 and Sec. IV B). In this configuration, the only nonzero component of the corrector $\boldsymbol{\chi}$ is χ_z ($\chi_x = 0 = \chi_y$) [17]. We can explain the vanishing of the components χ_x

and χ_y heuristically by resorting to the above boundary-value problem. Simply notice that each of these components (χ_i for $i = x, y$) satisfies the Laplace equation with *homogeneous* (forcing-free) boundary conditions across the surface Σ and along the nanoribbon edges which form the boundary of Σ. More precisely, $\nabla_\parallel \cdot \boldsymbol{\tau}_i = 0$ on the right-hand side of condition (C3) for all i; and $\boldsymbol{n} \cdot \boldsymbol{\tau}_i = 0$ for $i = x, y$ in Eq. (C4). Hence, by the expected uniqueness of the solution to the cell problem for χ_i, we have $\chi_x = 0 = \chi_y$. In contrast, χ_z is nonzero because $\boldsymbol{n} \cdot \boldsymbol{\tau}_z = \pm 1$ along the edges. Thus, the solution to the Laplace equation for χ_z is affected by the forcing term in the requisite boundary condition along the edges.

Hence, for the nanoribbon setting, Eq. (6) implies that the effective permittivity tensor $\underline{\varepsilon}^{\text{eff}}$ is represented by a diagonal matrix with distinct elements $\underline{\varepsilon}^{\text{eff}} = \text{diag}(\varepsilon_x^{\text{eff}}, \varepsilon_y^{\text{eff}}, \varepsilon_z^{\text{eff}})$ and $\varepsilon_x^{\text{eff}} \neq \varepsilon_y^{\text{eff}} \neq \varepsilon_z^{\text{eff}} \neq \varepsilon_x^{\text{eff}}$; see Sec. IV B for more details. This observation motivates the simplified but practically useful analysis of Sec. IV A.

We note in passing that, if needed, Eq. (C1) combined with the above boundary-value problem for $\boldsymbol{\chi}$ can be readily extended to a more general setting involving tensor-valued and spatially dependent material models for permittivitiy $\underline{\varepsilon}(\omega, \boldsymbol{r})$ and surface conductivity $\underline{\sigma}(\omega, \boldsymbol{r})$ [17]. In this paper, however, we restrict the discussion to the more practical situation of homogenization effects due to the sheet geometry alone.

[1] L. E. F. Foa Torres, S. Roche, and J.-C. Charlier, *Introduction to Graphene-Based Nanomaterials: From Electronic Structure to Quantum Transport* (Cambridge University Press, Cambridge, UK, 2014).

[2] A. K. Geim and I. V. Grigorieva, Van der Waals heterostructures, Nature (London) **499**, 419 (2013).

[3] A. H. Castro Neto, F. Guinea, N. M. R. Peres, K. S. Novoselov, and A. K. Geim, The electronic properties of graphene, Rev. Mod. Phys. **81**, 109 (2009).

[4] T. Low, A. Chaves, J. D. Caldwell, A. Kumar, N. X. Fang, P. Avouris, T. F. Heinz, F. Guinea, L. Martín-Moreno, and F. Koppens, Polaritons in layered two-dimensional materials, Nat. Mater. **16**, 182 (2017).

[5] K. S. Novoselov, V. I. Fal'ko, L. Colombo, P. R. Gellert, M. G. Schwab, and K. Kim, A roadmap for graphene, Nature (London) **490**, 192 (2012).

[6] Z. Q. Li, E. A. Henriksen, Z. Jiang, Z. Hao, M. C. Martin, P. Kim, H. L. Stormer, and D. N. Basov, Dirac charge dynamics in graphene by infrared spectroscopy, Nat. Phys. **4**, 532 (2008).

[7] S. Kim, M. S. Jang, V. W. Brar, K. W. Mauser, L. Kim, and H. A. Atwater, Electronically tunable perfect absorption in graphene, Nano Lett. **18**, 971 (2018).

[8] S. Dai, Q. Ma, M. K. Liu, T. Andersen, Z. Fei, M. D. Goldflam, M. Wagner, K. Watanabe, T. Taniguchi, M. Thiemens, F. Keilmann, G. C. A. M. Janssen, S.-E. Zhu, P. Jarillo-Herrero, M. M. Fogler, and D. N. Basov, Graphene on hexagonal boron nitride as a tunable hyperbolic metamaterial, Nat. Nanotechnol. **10**, 682 (2015).

[9] A. Nemilentsau, T. Low, and G. Hanson, Anisotropic 2D Materials for Tunable Hyperbolic Plasmonics, Phys. Rev. Lett. **116**, 066804 (2016).

[10] M. Mahmoodi, S. H. Tavassoli, O. Takayama, J. Sukham, R. Malureanu, and A. V. Lavrinenko, Existence conditions of high-k modes in finite hyperbolic metamaterials, Laser Photon. Rev. **13**, 1800253 (2019).

[11] H. Deng, Y. Chen, C. Huang, and F. Ye, Topological interface modes in photonic superlattices containing negative-index materials, Europhys. Lett. **124**, 64001 (2018).

[12] H. Deng, F. Ye, B. A. Malomed, X. Chen, and N. C. Panoiu, Optically and electrically tunable Dirac points and Zitterbewegung in graphene-based photonic superlattices, Phys. Rev. B **91**, 201402(R) (2015).

[13] S. V. Zhukovsky, A. Andryieuski, J. E. Sipe, and A. V. Lavrinenko, From surface to volume plasmons in hyperbolic metamaterials: General existence conditions for bulk high-$\boldsymbol{k}$ waves in metal-dielectric and graphene-dielectric multilayers, Phys. Rev. B **90**, 155429 (2014).

[14] M. Maier, M. Mattheakis, E. Kaxiras, M. Luskin, and D. Margetis, Universal behavior of dispersive Dirac cone in gradient-index plasmonic metamaterials, Phys. Rev. B **97**, 035307 (2018).

[15] T. C. Choy, *Effective Medium Theory: Principles and Applications* (Clarendon, Oxford, UK, 1999), Chap. 3.

[16] G. Pavliotis and A. M. Stuart, *Multiscale Methods: Averaging and Homogenization* (Springer, Berlin, 2007).

[17] M. Maier, M. Mattheakis, E. Kaxiras, M. Luskin, and D. Margetis, Homogenization of plasmonic crystals: Seeking the epsilon-near-zero effect, Proc. R. Soc. A **475**, 20190220 (2019).

[18] H. Yan, X. Li, B. Chandra, G. Tulevski, Y. Wu, M. Freitag, W. Zhu, P. Avouris, and F. Xia, Tunable infrared plasmonic devices using graphene/insulator stacks, Nat. Nanotechnol. **7**, 330 (2012).

[19] B. Yao, Y. Liu, S.-W. Huang, C. Choi, Z. Xie, J. F. Flores, Y. Wu, M. Yu, D.-L. Kwong, Y. Huang, Y. Rao, X. Duan, and C. W. Wong, Broadband gate-tunable terahertz plasmons in graphene heterostructures, Nat. Photonics **12**, 22 (2018).

[20] P. Ma, Y. Salamin, B. Baeuerle, A. Josten, W. Heni, A. Emboras, and J. Leuthold, Plasmonically enhanced graphene photodetector featuring 100 gbit/s data reception, high responsivity, and compact size, ACS Photonics **6**, 154 (2019).

[21] A. Nematpour, N. Lim, A. Piegari, L. Lancellotti, G. Hu, and M. L. Grilli, Experimental near infrared absorption enhancement of graphene layers in an optical resonant cavity, Nanotechnology **30**, 445201 (2019).

[22] A. Kumar, T. Low, K. H. Fung, P. Avouris, and N. X. Fang, Tunable light-matter interaction and the role of hyperbolicity in graphene-hBN system, Nano Lett. **15**, 3172 (2015).

[23] H. Hu, X. Yang, X. Guo, K. Khaliji, S. R. Biswas, F. J. G. de Abajo, T. Low, Z. Sun, and Q. Dai, Gas identification with graphene plasmons, Nat. Commun. **10**, 1131 (2019).

[24] I.-H. Lee, D. Yoo, P. Avouris, T. Low, and S.-H. Oh, Graphene acoustic plasmon resonator for ultrasensitive infrared spectroscopy, Nat. Nanotechnol. **14**, 313 (2019).

[25] J. Si and C. Sun, On the optical performance of composite structures of graphene and photonic crystals at infrared wavelengths, J. Appl. Phys. **122**, 133104 (2017).

[26] H. Hu, X. Guo, D. Hu, Z. Sun, X. Yang, and Q. Dai, Flexible and electrically tunable plasmons in graphene– mica heterostructures, Adv. Sci. **5**, 1800175 (2018).

[27] S. Kim, S. G. Menabde, V. W. Brar, and M. S. Jang, Functional mid-infrared polaritonics in van der Waals crystals, Adv. Opt. Mater. **8**, 1901194 (2020).

[28] P. Yeh, *Optical Waves in Layered Media*, 2nd ed. (Wiley, Hoboken, NJ, 2005), Chap. 5.

[29] H. A. Haus, *Waves and Fields in Optoelectronics* (Prentice Hall, Englewood Cliffs, NJ, 1984), Chap. 5.

[30] M. Mattheakis, C. A. Valagiannopoulos, and E. Kaxiras, Epsilon-near-zero behavior from plasmonic Dirac point: Theory and realization using two-dimensional materials, Phys. Rev. B **94**, 201404(R) (2016).

[31] M. Maier, D. Margetis, and M. Luskin, Dipole excitation of surface plasmon on a conducting sheet: Finite element approximation and validation, J. Comput. Phys. **339**, 126 (2017).

[32] M. Silveirinha and N. Engheta, Tunneling of Electromagnetic Energy Through Subwavelength Channels and Bends Using ϵ-Near-Zero Materials, Phys. Rev. Lett. **97**, 157403 (2006).

[33] X. Huang, Y. Lai, Z. H. Hang, H. Zheng, and C. T. Chan, Dirac cones induced by accidental degeneracy in photonic crystals and zero-refractive-index materials, Nat. Mater. **10**, 582 (2011).

[34] P. Moitra, Y. Yang, Z. Anderson, I. I. Kravchenko, D. P. Briggs, and J. Valentine, Realization of an all-dielectric zero-index optical metamaterial, Nat. Photonics **7**, 791 (2013).

[35] Y. Li, S. Kita, P. Muñoz, O. Reshef, D. I. Vulis, M. Yin, M. Lončar, and E. Mazur, On-chip zero-index metamaterials, Nat. Photonics **9**, 738 (2015).

[36] M. Mattheakis, M. Maier, W. X. Boo, and E. Kaxiras, Graphene epsilon-near-zero plasmonic crystals, in *Proceedings of the Sixth Annual ACM International Conference on Nanoscale Computing and Communication, NANOCOM '19* (ACM, New York, 2019), pp. 2:1–2:6.

[37] A. M Urbas *et al.*, Roadmap on optical metamaterials, J. Opt. **18**, 093005 (2016).

[38] T. Galfsky, E. E. Narimanov, and V. M. Menon, Enhanced spontaneous emission in photonic hypercrystals, in *Frontiers in Optics 2015*, OSA Technical Digest (Optical Society of America, Washington, DC, 2015), paper FW6A.3, pp. 1, 2.

[39] C. L. Cortes, W. Newman, S. Molesky, and Z. Jacob, Quantum nanophotonics using hyperbolic metamaterials, J. Opt. **14**, 063001 (2012).

[40] C. L. Cortes, W. Newman, S. Molesky, and Z. Jacob, Corrigendum: Quantum nanophotonics using hyperbolic metamaterials, J. Opt. **16**, 129501 (2014).

[41] A. Lucas and K. C. Fong, Hydrodynamics of electrons in graphene, J. Phys.: Condens. Matter **30**, 053001 (2018).

[42] M. Maier, D. Margetis, and M. Luskin, Generation of surface plasmon-polaritons by edge effects, Commun. Math. Sci. **16**, 77 (2018).

[43] C. L. Davies, J. B. Patel, C. Q. Xia, L. M. Herz, and M. B. Johnston, Temperature-dependent refractive index of quartz at terahertz frequencies, J. Infrared Millim. Te. **39**, 1236 (2018).

[44] T. Chang, X. Zhang, X. Zhang, and H.-L. Cui, Accurate determination of dielectric permittivity of polymers from 75 GHz to 1.6 THz using both S-parameters and transmission spectroscopy, Appl. Opt. **56**, 3287 (2017).

[45] P. Halevi, A. A. Krokhin, and J. Arriaga, Photonic Crystal Optics and Homogenization of 2D Periodic Composites, Phys. Rev. Lett. **82**, 719 (1999).

[46] Nagaraj and A. A. Krokhin, Long-range surface plasmons in dielectric-metal-dielectric structure with highly anisotropic substrates, Phys. Rev. B **81**, 085426 (2010).